SYNCHROTRON-BASED IMAGING AND TOMOGRAPHY OF HYDROGEL SCAFFOLDS FOR TISSUE ENGINEERING

A Thesis Submitted to the College of

Graduate Studies and Research

In Partial Fulfillment of the Requirements

For the Degree of Master of Science

In the Department of Mechanical Engineering

University of Saskatchewan

Saskatoon

By

CHENGLIN LIU

PERMISSION TO USE

In presenting this thesis in partial fulfilment of the requirements for a Postgraduate degree from the University of Saskatchewan, I agree that the Libraries of this University may make it freely available for inspection. I further agree that permission for copying of this thesis in any manner, in whole or in part, for scholarly purposes may be granted by the professor or professors who supervised my thesis work or, in their absence, by the Head of the Department or the Dean of the College in which my thesis work was done. It is understood that any copying or publication or use of this thesis or parts thereof for financial gain shall not be allowed without my written permission. It is also understood that due recognition shall be given to me and to the University of Saskatchewan in any scholarly use which may be made of any material in my thesis.

Requests for permission to copy or to make other use of material in this thesis in whole or part should be addressed to:

Head of the Department of Mechanical Engineering

57 Campus Drive

University of Saskatchewan

Saskatoon, Saskatchewan S7N 5A9

ABSTRACT

Tissue engineering aims to repair damaged tissues and organs by building artificial tissues using scaffolds. Recently, scaffolds made from hydrogels have shown great potential to encapsulate living cells to control the spatial distribution of the cells for various tissue engineering applications. Due to high water content, hydrogels are hard to visualize in aqueous environments, which is, however, essential to track the success of hydrogel scaffolds in their applications. Nowadays, synchrotron-based imaging holds huge promise for non-invasive high-resolution visualization of the cell-scaffold constructs *in vitro* and *in vivo*. The research presented in this thesis was aimed at preforming a preliminary study on the use of synchrotron-based imaging techniques *in vitro* to visualize scaffolds and cells in tissue engineering. Particularly, scaffolds were fabricated from alginate hydrogels and imaged in aqueous solution by means of various synchrotron imaging techniques.

First, K-edge subtraction (KES) imaging with computed tomography (CT) visualized alginate scaffolds were taking advantage of barium contrast agents. In contrast to conventional physical methods, a novel chemical method to incorporate barium with alginate scaffolds was applied for the scaffold visualization. Second, chitosan micro-spheres (CMs) were encapsulated in alginate scaffolds as contrast agent for in-line phase contrast imaging (PCI). Chitosan can be visualized more easily by PCI than alginate so that the distribution of CMs can indicate the shape of the scaffolds. Lastly, a combination of absorption imaging and PCI were used to visualize both the encapsulated cells and alginate scaffolds. To visualize the cells, gold nano-particles (GNPs) were employed as a marker to generate absorption contrast. For the PCI of the scaffolds, samples of different alginate cross-linking levels were tested and examined for comparison.

KES with barium contrast agents showed promising imaging results. The scaffolds which incorporated barium by a novel chemical method were imaged with brighter and highlighted edges

than the physical method. Alginate/CMs scaffolds can be visualized by PCI and can also be clearly imaged if combining it with CT. It was found that increasing the concentration of CMs within scaffolds can improve the images, but can also inversely affect the fabrication of scaffolds. For cell/scaffold visualization, absorption radiography can produce some dark spots in the images, however those spots cannot be recognized as either GNPs marked cells or noise at the present study, suggesting that further research is needed. The visibility of the scaffold by PCI is found to mainly depend on the cross-linking time of alginate. Longer cross-linking time can help improve the contrast by PCI-CT for quantitative analysis of the structure.

The present study shows that different synchrotron imaging schemes based on KES and PCI have potential to visualize hydrogel scaffolds in aqueous environments. The methods and findings of the present study would facilitate the development of non-invasive methods to visualize tissue scaffolds and cells in the future.

ACKNOWLEDGMENTS

First, I'd like to express my appreciation to my supervisors, Dr. Daniel Chen and Dr. Jim Bugg, for their encouragement and instruction through my research project. I'm grateful for their supervision.

Also, I would like to thank my Advisory Committee members, Dr. James Johnston and Dr. Donald Bergstrom, for their kind examination and advice on my research work.

I also want to express my gratitude to Dr. Dean Chapman (Department of Anatomy and Cell Biology) and Dr. Ning Zhu (Canadian Light Source Inc.) for providing me with valuable comments and research instruments. Such research technicians as Tangyne Berry, Doug Bitner, and CLS beamline scientists as Dr. George Belev and Adam Webb have provided me with lots of technical support for my experiment, without which I could not have finished my research work.

I would also like to acknowledge the support of a scholarship from the CIHR-THRUST program, as well as the College of Graduate Studies and Research of the University of Saskatchewan.

TABLE OF CONTENTS

LIST OF FIGURES

Figure Page

LIST OF ACRONYMS

3D	Three dimensional
BM	Bend magnet
BMIT	Biomedical Imaging and Therapy
CLS	Canadian Light Source
CLSM	Confocal laser scanning microscopy
CM	Chitosan microsphere
CT	Computed tomography
DMEM	Dulbecco's Modified Eagle Medium
ECM	Extracellular matrix
FBP	Filtered-back projection
FBS	Fetal bovine serum
FEA	Finite element analysis
FV	Field of view
GNP	Gold nano-particle
KES	K-edge subtraction
MIR	Multiple image radiography
MRI	Magnetic resonance imaging
PBS	Phosphate buffered saline
PCI	Phase contrast imaging
SD	Sample-detector distance
SEM	Scanning electron microscopy
SNR	Signal-to-noise ratio
SR	Synchrotron radiation
TE	Tissue engineering

CHAPTER 1
INTRODUCTION

1.1 Background

1.1.1 Tissue Engineering

Tissue engineering (TE) is an interdisciplinary application of biology, engineering, medicine and material science. In TE, biodegradable and biocompatible materials are used to form artificial extracellular matrices (ECM) by engineering approaches, in order to develop biological substitutes that restore, maintain or replace a tissue or whole organ. To this end, cells could be isolated from healthy sites of patients, proliferated *in vitro*, incorporated with ECM, and eventually implanted back into the patient to correct the functional defects (Figure 1). TE promises to alleviate the shortage of tissue/organ donations and to eliminate immunological rejections.

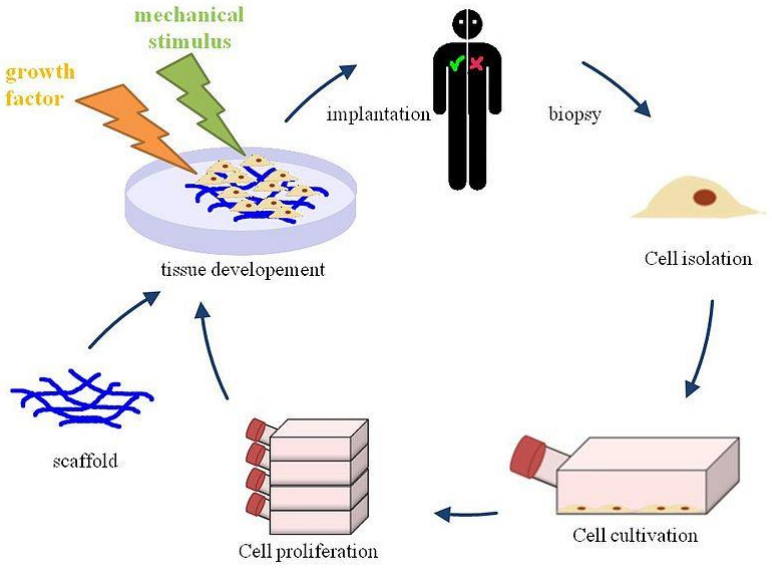

Figure 1. The principle of tissue engineering

1.1.2 Scaffolds

Tissue engineered scaffolds are three-dimensional (3D) artificial structures employed as ECM, which are used to promote tissue regeneration/repair by supporting cell migration, growth and differentiation; transporting nutrients and wastes; and providing adequate mechanical strength required during transplantation and implantation *in vivo*. For their vital role in TE, scaffolds must possess the following biological, chemical and physical properties.

First, biocompatibility is essential for any scaffold to maintain cell viability and to avoid negative interaction with surrounding tissues. Such a requirement is typically met by properly selecting biomaterials for the scaffold fabrication. There are different kinds of biocompatible biomaterials; classified as natural and synthetic biopolymers. Natural biopolymers, including collagen, chitosan, alginate and silk, are the ones derived naturally from a biological environment, thus having good biocompatibility. Synthetic polymers are man-made and generally have lower biocompatibility but stronger mechanical properties. Some typical synthetic polymers used in TE include polylactides, polycaprolactone, polyurethanes and etc.

Second, biodegradability is essential for the scaffold to promote the regeneration of new tissue. During this process, tissue regeneration and scaffold degradation are closely matched. If degradation occurs too quickly, the scaffolds will simply dissolve, thus not being able to provide support for the regeneration of new tissue as required. If degradation is too slow, a buildup of ECM will occur in the pericellular regions, which not only affects tissue growth, but may also influence cell function [1]. Ideally, the rate of scaffold degradation should be matched with the rate of new tissue formation. The degradation profile can be controlled through a variety of mechanisms [2]. These factors will directly influence the structural evolution of the scaffolds, which subsequently impact the spatial deposition of newly synthesized tissues.

Architecture and structural mechanics are also crucial for tissue engineering scaffolds. Porosity can be considered as the main factor of architecture. High porosity (e.g. 90%) may provide a great pore volume for cell infiltration and ECM formation, as well as maximizing the diffusion and exchange of nutrients (e.g. oxygen, glucose) [3]. The morphological architecture of scaffolds is mainly determined by the scaffold fabrication techniques. Some examples produced by different fabrication techniques are shown in Figure 2. The mechanical properties of a porous solid depend mainly on its relative density, the properties of the material that make up the pore edges or walls and its anisotropic nature [4]. Hence, there is often a compromise between porosity and scaffold mechanical properties, i.e., high porosity decreases mechanical properties [3].

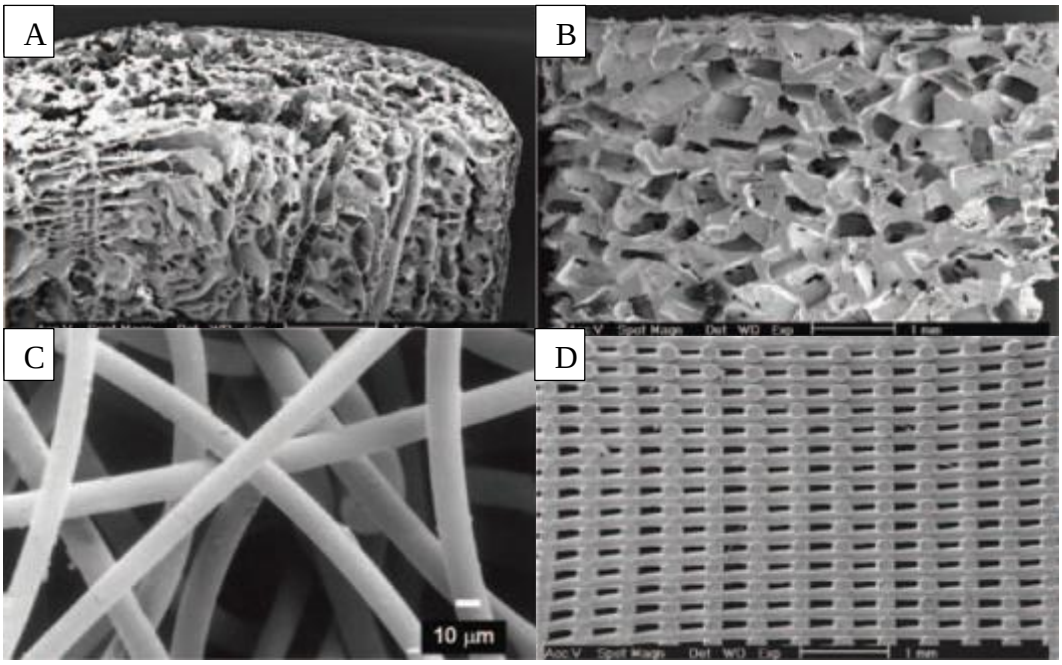

Figure 2. Scanning electron micrographs of scaffolds produced using various fabrication techniques. (A) liquid-solid phase separation and freeze-drying using 1,4-dioxane (PEGT/PBT), (B) compression molding and porogen leaching (PEGT/PBT), (C) nonwoven polylactic acid (PLA) mesh, (D) 3D plotting of PEGT/PBT scaffold [5].

1.1.3 Hydrogels

Hydrogels are attractive biomaterials to meet the requirements of scaffolds for tissue engineering [6-10]. A biomaterial that contains over 20wt% water and maintains a permanent 3D structure may be considered a hydrogel [11]. Hydrogels are water swellable (yet water insoluble) cross-linked networks that exhibit high water content and tissue-like elastic properties. Hydrogels also offer a sufficient diffusion rate of hydrophilic substrates for the encapsulation of living cells. These attributes make hydrogels ideal candidates for scaffold materials to encapsulate cells [8].

Many hydrogel macroscopic properties are important in scaffold design. These properties are closely related to the degree of crosslinking; an increase in the crosslinking density results in gels with higher mechanical strengths, but lower swelling capabilities and decreased mesh sizes. Although encapsulated cells benefit from high water content for transport of nutrients and waste, a hydrogel will not maintain mechanical integrity if it is highly diluted [11]. Therefore, there is a balance in designing a hydrogel with appropriate properties that exhibit sufficient mechanical integrity without sacrificing cell viability and tissue growth. Several studies have demonstrated that the hydrogel structure dramatically influences the distribution of newly synthesized matrix molecules within the hydrogel, playing a pivotal role in 3D macroscopic tissue development [12, 13]. In addition to the structure, hydrogel chemistry plays an important role in cell function and initial cell survival. Alternative strategies have developed natural hydrogel environments by mimicking the native ECM, which not only promotes cell–matrix interactions with the hydrogel but also sequesters important growth factors that can augment tissue growth [14].

In this thesis, alginate as a natural hydrogel is used as the scaffold material. Alginate has been widely used in medical applications due to its biocompatibility and biodegradation properties [15, 16]. Alginate is derived from sea algae and is composed of linear block copolymers of 1-4 linked b-D-mannuronic acid (M) and a-L- guluronic acid (G). Alginate can be chemically cross-linked

by means of divalent cations (like Ca^{2+}) in aqueous solutions. The gelation and cross-linking of the hydrogel is mainly caused by the exchange of sodium ions from the guluronic acids with the divalent cations and the stacking of these guluronic groups to form "egg-box" structures [17]. Scaffolds made of alginate cross-linked with calcium chloride ($CaCl_2$) can support cells and provide pores for them to penetrate through [18]. The scaffolds were fabricated by a 3D plotting method [19] to control their shape and architecture (Figure 3). Compared with dispensing in air, dispensing alginate into the cross-linker solution is more complicated due to the need to coordinate the dispensing flow rate and the cross-linking rate. Otherwise, the fabricated scaffolds may suffer from structural defects such as discontinuous strands, leading to the collapse of the scaffold.

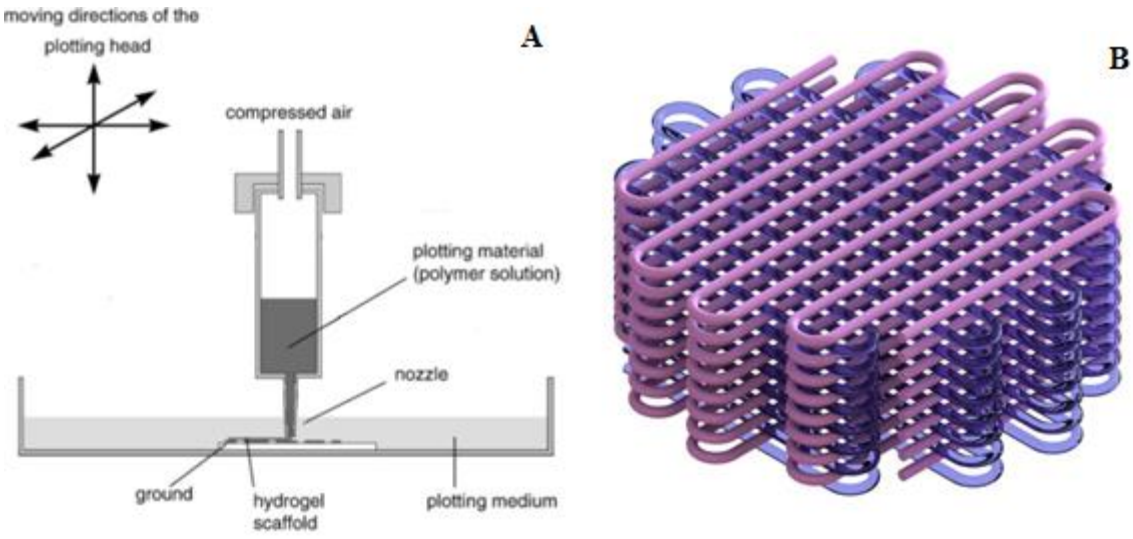

Figure 3. A) 3D plotting method [19] and B) grid patterned 3D scaffold.

1.1.4 Visualization of Scaffolds and Cells in Tissue Engineering

Visualization of tissue scaffolds is essential to acquire knowledge of the scaffold structure as well as its static and dynamic interaction with cells during the healing process. Ideally, imaging techniques for TE are expected to capture: (1) the differentiation of cells, the degradation of scaffolds and the regeneration of tissue can be continuously monitored non-invasively without

tissue destruction; (2) cells incorporated into the scaffolds can be tracked and visualized; and (3) characteristics of scaffolds can be quantified and analyzed by 3D images [20]. For scaffold design and fabrication, visualization of scaffolds provides an effective approach to study the mechanical properties of scaffolds non-destructively by means of finite element analysis (FEA), thus allowing for the better design and fabrication of scaffolds [21, 22].

A number of visualization techniques have been applied in TE, including scanning electron microscopy (SEM), confocal laser scanning microscopy (CLSM), magnetic resonance imaging (MRI), as well as synchrotron radiation (SR) X-ray imaging and computed tomography (CT). These techniques and their application to the visualization of scaffolds and cells are briefly reviewed in the following section.

1.2 Literature Review on the visualization of scaffolds and cells

1.2.1 SEM

SEM is a widely used visualization technique for micro-morphology analysis in physics, biology, and engineering. The most important advantage of SEM is its high spatial resolution which can achieve the level of nanometers. As an example (shown in Figure 4) SEM can reveal the structural features of scaffolds including porosity [23, 24], strand dimensions [25], cross-sectional area and interconnectivity [26, 27]. Also, SEM can be used to monitor the cells' attachment and interaction with the surface of the scaffold [28, 29].

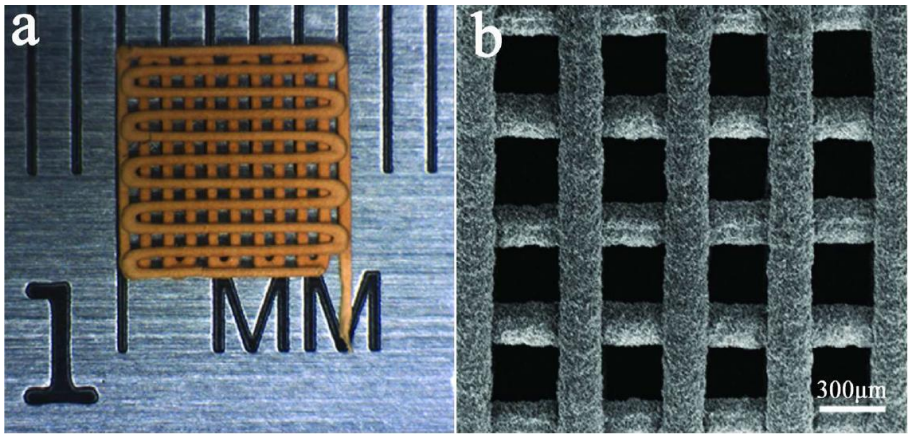

Figure 4. Images of the PLLA/chitosan scaffold from (a) camera and (b) SEM [23]

Conventional SEM is subject to the limitation that samples have to be electrically conductive. Therefore, biological samples have to be coated with a heavy metal like gold, gold/palladium alloy, platinum, or osmium [30]. Environmental SEM (ESEM) has been developed to image non-conductive samples without coating [31]. Also, SEM techniques can only reveal the surface images of the specimens, which means only two dimensional images can be obtained. Hence, 3D images and non-invasive imaging cannot be achieved by SEM.

1.2.2 CLSM

CLSM is a visualization technique to obtain high resolution images from selective depth of specimens [32]. The major character of CLSM is to obtain images of the specimen from selected depths of focus. Since the images are acquired plane-by-plane, 3D images can be reconstructed to reveal the topology of the sample. By taking advantage of the 3D visualization ability of CLSM, the 3D morphological features of the TE scaffolds can be evaluated for better understanding of the contribution to tissue regeneration (Figure 5)[33, 34]. However, the visualization ability of CLSM is limited by the focal depth of the laser, which varies from 10 – 300 micron. Hence, non-invasive visualization of TE scaffolds is difficult to achieve by CLSM.

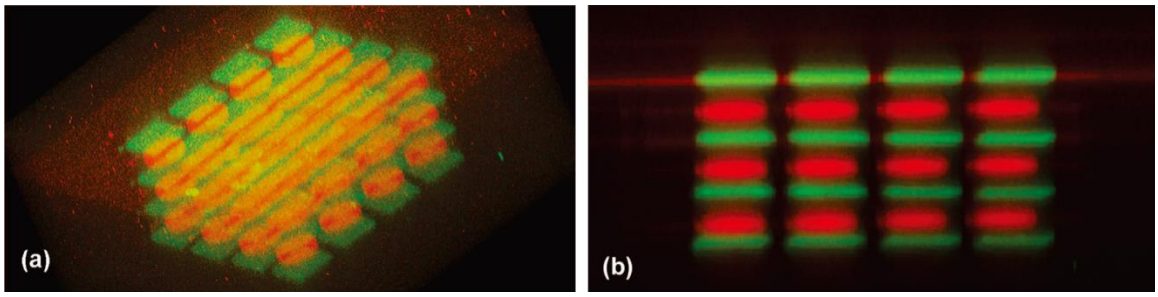

Figure 5. (a) Oblique and (b) side views of the 4 × 4 × 4 array of 3D patterned squares [34]

1.2.3 MRI

MRI has been widely applied in medical imaging, especially for soft tissues. This imaging technique utilizes the resonant frequency of excited hydrogen atoms to generate contrast from the differences in water content of different tissues. According to the mechanism, the key advantage of MRI is to generate 3D images of soft tissues without any radiation dose. For TE applications, MRI is usually applied to acquire morphological data of the damaged tissue in order to design the prototype scaffold [35-37]. MRI is also a promising imaging method to visualize hydrogel *in vivo* for its ability to distinguish substances containing water. However, MRI cannot reveal the fine micro structure of the scaffolds due to its low resolution [37].

1.2.4 Synchrotron X-ray Imaging

X-rays are a series of electromagnetic radiations with wavelengths generally in the 0.01 to 10 nm range. The high energy of these photos make X-rays highly penetrating with relatively low absorption. These characteristics can be utilized for imaging techniques to visualize the internal details of an object.

X-rays are usually generated from two kinds of sources. An X-ray tube is a conventional source, which can generate X-rays rapidly at low cost. X-ray tubes use a high voltage to accelerate the electrons released by a hot cathode to a high velocity. The high-velocity electrons collide with a

metal target, the anode, creating the X-rays [38]. X-ray tubes can be widely used in common applications, however they suffer from several limitations in research applications. Since fluorescence emissions from anode produce mostly monochromatic x-rays, the beam obtained is not continuously tunable. Also, the X-rays are emitted in all directions without control (Figure 6), hence they need to be redirected into a collimated beam before use.

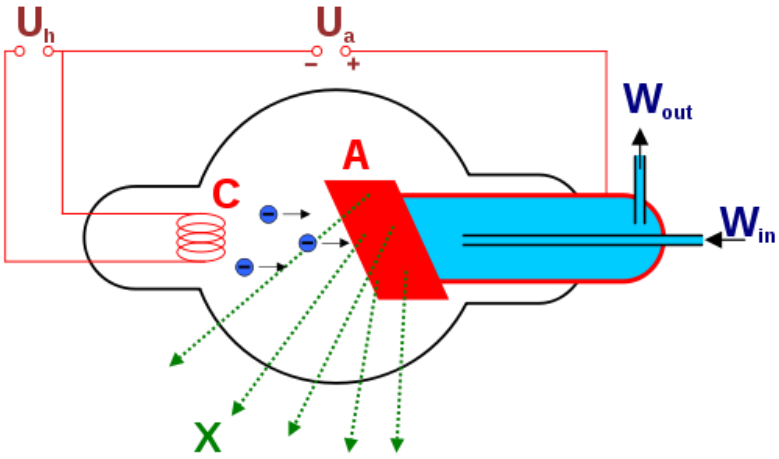

Figure 6. Coolidge Tube Scheme (A: anode, C: cathode, X: x-rays, U: voltage, W: water).

A synchrotron, a type of cyclic accelerator; is another source of X-rays. Electrons are accelerated to almost light speed and generate electromagnetic radiation when their velocity vectors are altered by the bending magnets or insertion devices. Figure 7 is a schematic of a typical synchrotron facility. The radiation generated by accelerated electrons in a synchrotron radiation (SR) can be regarded as a much better light source. Compared with an X-ray tube, synchrotron radiation can provide a tunable beam with a much higher intensity and brightness, which can enhance imaging techniques with higher resolution and higher signal-to-noise ratio (SNR). Besides, polarized light from synchrotron radiation is naturally collimated in the vertical plane, which can be well matched to many precise imaging facilities, especially for research purposes [39]. Based on these advantages, different imaging techniques including absorption edge subtraction, in-line

phase contrast imaging, and diffraction enhanced imaging are available by using a synchrotron radiation source.

Figure 7. Synchrotron light source concept schematic diagram

Since high-energy radiation will interact with biological tissue and cause damage to cells, dose is an important factor in medical imaging techniques which use X-rays. Normally the absorbed dose will be primarily considered in medical imaging. Absorbed dose is defined as the energy deposited per mass of material in which the energy is deposited. For matter exposed to radiation of a single energy, the maximum dose occurs at the surface which can be calculated as:

$$D_s = \frac{N_0 E}{A}\mu_{\mathrm{A}} \tag{1}$$

where E is the photon energy, A is the cross-sectional area of the region the beam hits, N_0 is the number of photons, and μ_A is the mass absorption coefficient, which is specific to a material and is related to the cross section per atom. μ_A accounts for the absorbed X-rays which result in energy deposition, which follows

$$\mu_A \propto \frac{Z^3}{E^3} \quad (2)$$

where Z is the atomic number. Therefore the surface dose is proportional to $\frac{1}{E^2}$, which means the higher energy X-ray will produce much lower dose.

Regular X-ray imaging provides two-dimensional radiographic images. In order to obtain three dimensional images of the internal structure, CT is utilized by computer processing of a large series of two-dimensional radiographic projections taken around a single axis of rotation [40]. The most significant advantage of CT is to observe the internal structure without any invasive destruction of the object. The combination of high-resolution synchrotron X-ray imaging and CT has become a promising approach for medical research. For tissue engineering, taking advantage of SR CT can not only investigate and improve the morphological design of the scaffold, but can also observe tissue regeneration and avoid invasive surgeries.

1.2.4.1 K-edge Subtraction

SR absorption contrast imaging has a similar set-up (Figure 8) as traditional clinical radiography using X-rays from an X-ray tube. The incoming white beam reflects on double crystal mono-chromators in order to select the target energy photons. Then the beam goes through the object and hits the planar detector. Hence, absorption contrast imaging uses the differences in absorption coefficients within the imaged object and obtains the attenuation contrast on the detector.

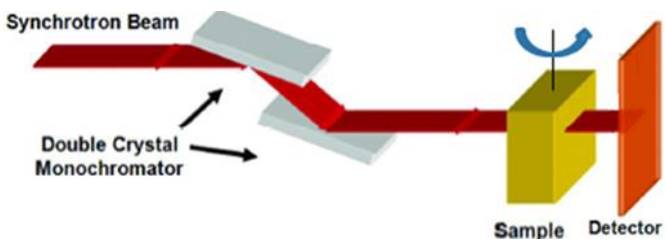

Figure 8. Schematic of SR absorption contrast imaging setup

Absorption edge subtraction imaging technique is an advanced imaging method which was developed from absorption contrast imaging. The images are taken near special photon energies, called absorption edges, which are sharp discontinuities in the X-ray absorption spectrum of a substance. These discontinuities occur where the absorbed photon energy corresponds to an electronic transition or ionization potential. For example, a photon with energy just above the binding energy of the electron is more likely to be absorbed than a photon with energy just below this binding energy. Hence, the absorption coefficient of a substance suddenly increases. When two images are taken just above and below the absorption edge of an element, the intensities of the substance with this element distinguish significantly while the intensities of the remaining parts are almost the same [41]. Taking advantage of this, these substances can be employed as contrast agents so that the subtraction of the intensity of corresponding pixels of the two images can remove the background and highlight the parts marked by the contrast agents. As long as the target object is completely bonded with the contrast agents, the absorption edge subtraction image of the contrast agent can reveal a high-quality visualization of the object (Figure 9). Usually, the K-edge is the greatest absorption edge for most elements. Therefore, the K-edge is the most widely used absorption edge so that the subtraction images can achieve higher contrast.

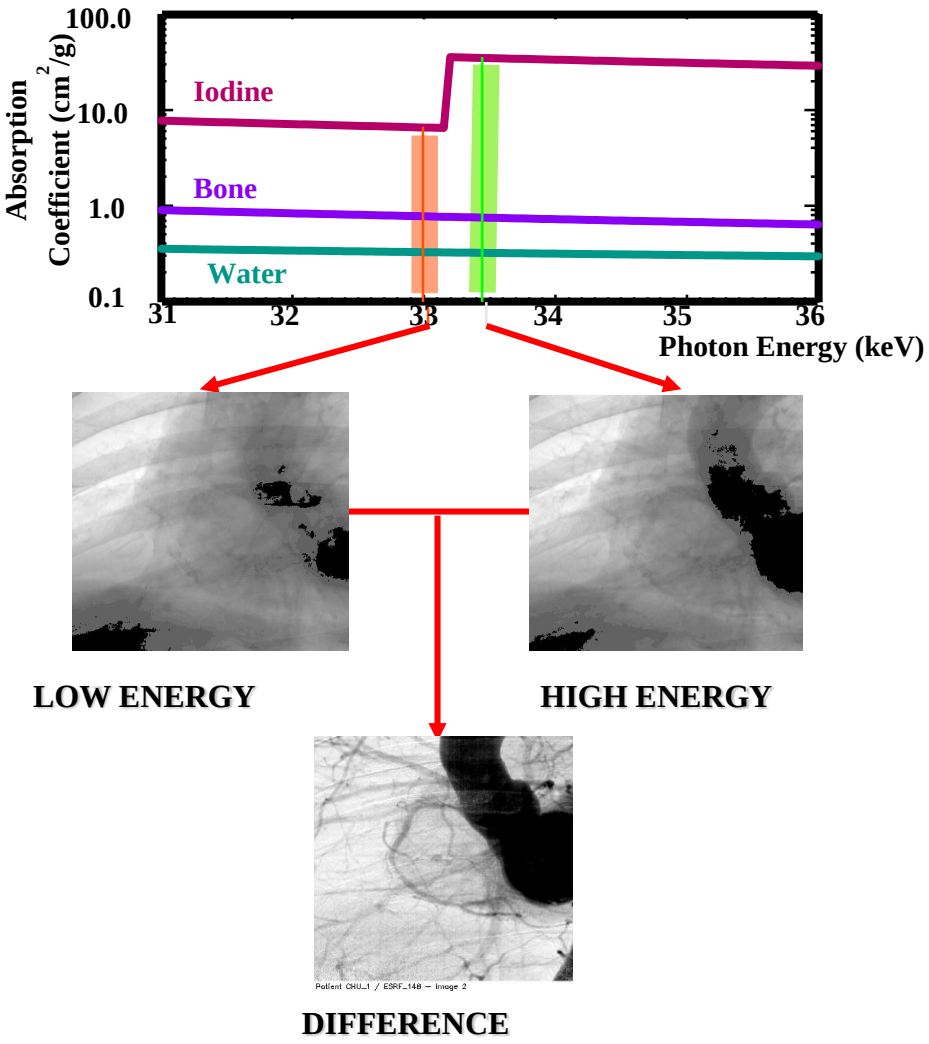

Figure 9. K-edge subtraction imaging – Coronary Angiography [42]

K-edge subtraction imaging is a promising visualization method employed for soft tissues, such as coronal angiography imaging [42], neurovascular angiography [43], and mammography [44]. Nevertheless, few applications of KES imaging for TE have been reported. Iodine and barium are the most common contrast media because of their strong X-ray absorption characteristics. However, iodine is normally considered the better option for *in vivo* imaging due to the toxicity of barium. In some specific research areas like islets transplantation, researchers have reported some positive results regarding the biocompatibility of barium compounds [45, 46]. These studies reveal

that the cytotoxicity of barium can be controlled, which demonstrates the potential for barium to be applied *in vivo* as a contrast agent for imaging.

1.2.4.2 Phase Contrast Imaging

Phase-contrast imaging is another major imaging technique using SR X-rays. Compared with the absorption imaging configuration, the distance between the sample and the detector is much larger (usually several meters) for in-line phase-contrast imaging (Figure 10). For absorption imaging, the detector is usually placed close to the sample in order to minimize the attenuation in the air. Thus, the major contrast is from X-rays absorbed by the sample. For in-line PCI, when X-rays transmit through the sample, the sample refracts the beam.

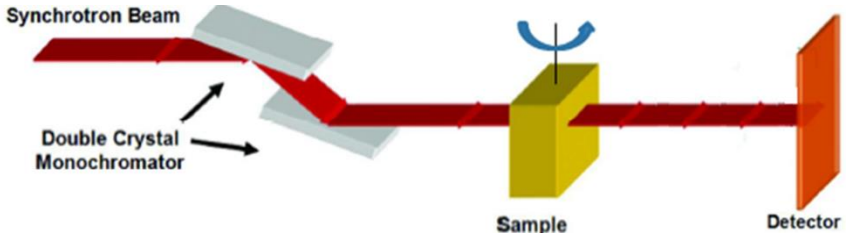

Figure 10. Schematic of SR phase-contrast imaging setup

As the distance between the sample and detector increases, the bending of the beam results in a conspicuous bias and leads to a greater intensity difference at the contours of the sample's image. According to Figure 11 [47], phase-contrast imaging takes advantage of the noticeable contrast from the refraction and results in better images than absorption [48]. Absorption imaging cannot distinguish many soft tissue lesions from normal tissue because there is little distinction of absorption coefficients. However, phase-contrast imaging can help to distinguish them by enhancing the contrast at the edges [49, 50].

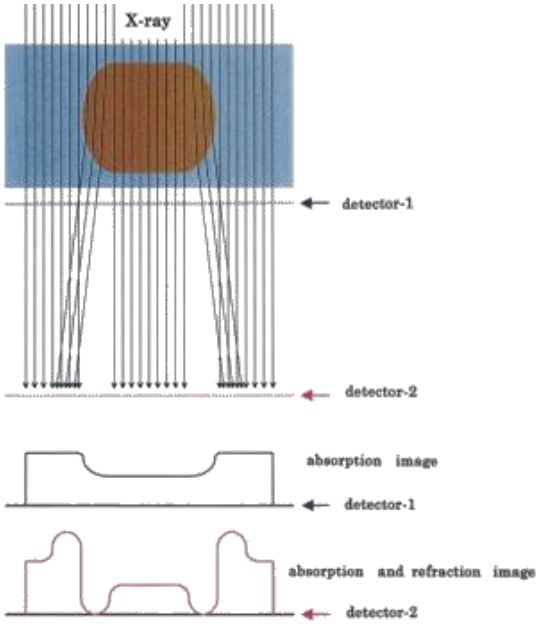

Figure 11. Principle of absorption imaging and refraction imaging [47]

The capability of PCI to differentiate between materials of similar density without contrast agents makes it attractive for *in vivo* imaging. Currently, most TE applications of PCI are mainly concerned with observing bone [51, 52] and cartilage [53]. Some groups have applied PCI to characterize the interconnectivity and porosity of hydroxyapatite scaffolds and to analyze a bio-membrane of poly (lactic acid) (PLA) [54, 55]. In these studies, specimens were imaged in air so that the significant differences of X-ray refractive index between soft tissue/scaffold and air can enhance the contrast. Shown in Figure 12, Eric *et al.* [56] reported the results of imaging hydrogel in a hydrated environment by multiple image radiography (MIR, an improved imaging technique based on PCI). However, the resolutions of their images were not high enough to reveal more morphological features.

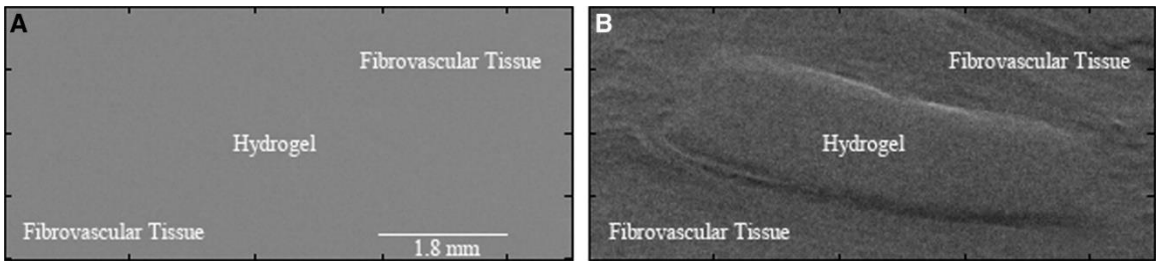

Figure 12. (A) Absorption and (B) refraction images of porous (74 μm) PEG hydrogels [56]

1.2.4.3 Cell imaging

Non-invasive cell tracking and imaging is an important goal for TE. The interaction between the cells, scaffolds and surrounding tissues can be monitored without destroying the body. To achieve this ultimate goal, several imaging techniques based on SR have been applied.

With the help of contrast agents, SRμCT (pixel sizes are in micrometer range) can reveal the 3D morphological features of labeled cells. Gold nano-particles (GNPs) are considered to be ideal marker due to their non-cytotoxicity and biocompatibility. Thurner *et al.* successfully obtained the cell volume and distribution data from SRμCT using gold-labeled foreskin fibroblasts and osteoblast-like cells on polymer scaffolds [57]. Also, some *ex vivo* SRμCT results illustrated clear GNPs labeled cells' distribution maps in rats' brains [58, 59]. A later study from Astolfo *et al.* [60] showed the comparison of *in vivo* and *ex vivo* SRμCT results of GNPs labeled cells (Figure 13). Although the *in vivo* image suffered from lower resolution due to the dose limitation, its great potential to visualize cells *in vivo* can be promoted in the future.

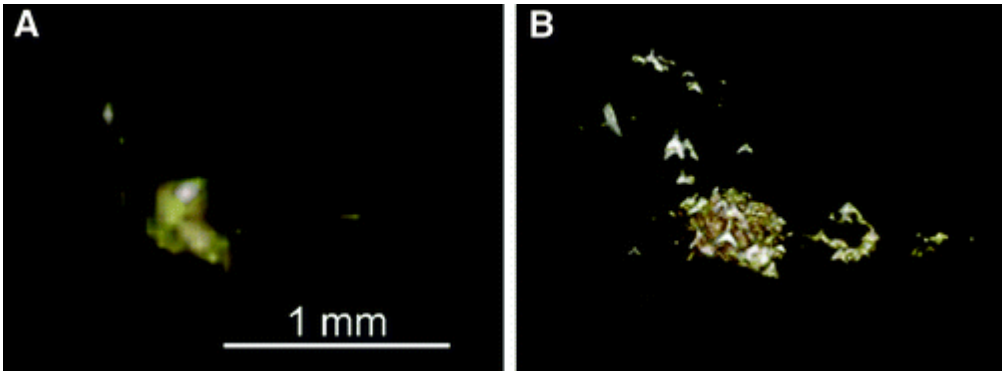

Figure 13. SRμCT rendered images of GNP labeled cells: (A) low dose *in vivo* (B) high dose *ex vivo* [60]

Another possible method to visualize cells *in vivo* is phase-contrast micro-tomography (PCμCT). Compared with SRμCT, the advantage of PCμCT is the absence of contrast agents. Zehbe *et al.* applied PCμCT to characterize the morphological features of cartilage cells [61]. Recently, Giuliani *et al.* [62] showed the potential of PCμCT to visualize polymer scaffolds and cells together with two different phases (Figure 14). This technique would be promising to illustrate the interactions between the scaffolds and cells.

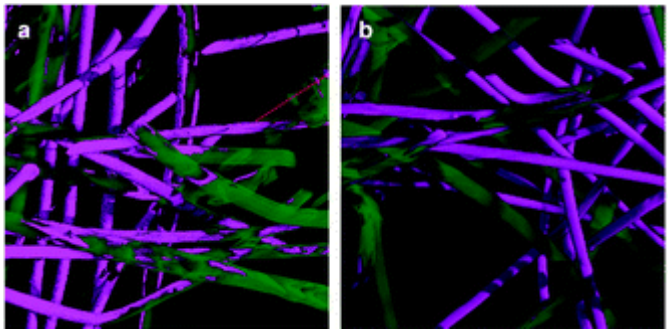

Figure 14. PCμCT of polyglycolic acid–polylactic acid scaffold and cells, PGA/PLLA fibers are colored in green, whereas the contrast produced by cells, cell clusters, and ECM layers are colored in magenta. (a) 6 days of culture; (b) 12 days of culture [62]

The limitation of these methods is that the micro–tomography technique can be only applied on small specimens. Thus *in vivo* imaging can only be employed for small animals like mice. Cell visualization techniques for large specimens are required.

1.3 Research Objectives

The main objective of this thesis is to visualize alginate scaffolds in aqueous environments by synchrotron X-ray imaging techniques to study the morphological properties of scaffolds. Three specific objectives are to be achieved in this research, which are presented below with the methods used.

1) Apply K-Edge Subtraction imaging to visualize hydrogel scaffolds with barium contrast agents. Scaffolds that incorporate the physical and chemical forms of barium of different concentrations are visualized for comparison. Projections are taken at energy levels below and above the K-edge of barium for computed tomography. 3D volume rendering is carried out from the reconstructed CT slices to obtain the inner structures.
2) Add chitosan microspheres into alginate scaffolds as contrast agents for in-line phase contrast imaging. Different quantities of microspheres are to be incorporated in scaffolds and compared with regard to the imagines obtained. Meanwhile, CT is also applied to obtain 3D images for analysis.
3) By combining two SR-based imaging techniques, introduce a method to visualize both alginate scaffolds and cells. Absorption radiography is applied to image GNPs labeled Schwann cells. With the same detector setting, in-line PCI is applied to visualize alginate scaffolds with different levels of cross-linking, but without any contrast agent. By combining cell images and scaffold images, tomography is applied to obtain the 3D visualization.

1.4 Organization of thesis

This thesis include five main chapters: 1) Introduction, 2) Synchrotron based K-edge subtraction imaging and tomography of alginate scaffolds, 3) Synchrotron based phase contrast imaging and tomography of alginate scaffolds with chitosan micro-spheres, 4) Synchrotron based phase contrast imaging and tomography of alginate scaffolds with gold labeled cells, and 5) Conclusion, discussion and future work.

The introduction chapter presents a background to the present work, which includes a literature review of various methods to visualize tissue scaffolds, the research objectives and organization of this thesis. The following three chapters present three pieces of research work to visualize scaffolds by means of synchrotron-based imaging techniques. Specifically, Chapter 2 demonstrates the KES imaging and CT for visualization of alginate scaffolds in water with two different methods to incorporate barium as contrast agent.

In Chapter 3, chitosan micro-spheres were fabricated and used in alginate scaffolds as contrast agents for phase contrast imaging. In-line PCI with CT was applied to monitor the distribution of chitosan micro-spheres and derive the 3D structure of the scaffold.

Chapter 4 presents a study on the visualization of alginate scaffolds with GNPs labeled cells. Using the same detector setting, the GNPs labeled cells were imaged by absorption radiography; while the alginate scaffolds were imaged by in-line PCI, in which alginate hydrogel with different levels of cross-linking were used. CT techniques were also applied to observe morphology of the scaffolds.

Chapter 5, presents the conclusions drawn from the present research, its limitations, and a discussion on possible improvements and developments in the future.

CHAPTER 2
SYNCHROTRON-BASED K-EDGE SUBTRACTION IMAGING AND TOMOGRAPHY OF ALGINATE SCAFFOLDS

2.1 Introduction

X-ray imaging is a common visualization method for both clinical diagnosis and biomaterial research. Conventional radiography is based on the contrast generated by X-ray absorption. Substances with low densities, like soft tissue and hydrogels, have similar absorption of X-ray, which makes it difficult to distinguish them from each other in radiography images. Low photon energy is usually employed to increase contrast in conventional radiography since the photoelectric absorption increases as the photon energy becomes low. However, this would cause a high level of X-ray dose absorbed by the samples being imaged.

The K-Edge subtraction imaging technique performs better than conventional radiography to enhance imaging contrast by taking advantages of contrast agents. The absorption of the structure marked with the contrast agent will increase significantly at a special photon energy (called K-edge), while the absorption changes little for the structures without the contrast agent. Subtraction of the two images above and below K-edge removes the background and the structure marked by the contrast agent is highlighted. Usually, the contrast agent is chosen as a large atomic number element thus its K-edge is high. Therefore, in K-edge subtraction (KES) imaging, absorption radiography is achieved with low dose and high quality.

Barium is one of the most commonly used contrast agents in X-ray radiography due to its strong X-ray absorption. The conventional form is barium sulfate ($BaSO_4$) [61, 62], which is insoluble, and, as such, toxic barium ions are not released. However, the insolubility of $BaSO_4$ makes it difficult to spread uniformly, especially in hydrogel. By taking advantage of barium's chemical properties, a novel method is presented in this chapter to image hydrogel scaffolds by KES.

Specifically, alginate scaffolds were imaged by KES using high energy X-ray from the Canadian Light Source (CLS). Barium was employed as a contrast element since its K-edge is high (37.441keV) and in the range of the beam-line's capability at CLS. Physical and chemical methods of incorporating barium into scaffolds were used and compared to each other. In the conventional physical method, $BaSO_4$ powder was mixed with alginate gels. The chemical method to incorporate barium was to cross-link barium ions to alginate. Different quantities of barium were applied for both methods to achieve the best image quality. Two images were taken above and below 37.441 keV and subtracted for each sample. The tomography scans of samples were applied at two energies as well in order to obtain KES-CT data for 3D analysis.

2.2 Materials and Methods

2.2.1 Chemicals

Alginate sodium (low viscosity, molecular weight range 12,000 ~ 80,000 Da), purchased from Sigma, was used for the scaffold fabrication. Barium sulfate (Sigma) was mixed with the alginate solution as a contrast agent. Barium chloride (Sigma) and calcium chloride (Sigma) was used to make the cross-link media. Poly-ethylenimine branched (PEI, Sigma) and glycerol (Sigma) were used to adjust the density and viscosity of the cross-link media.

2.2.2 Physical combination of barium and alginate

For the physical method, barium sulfate ($BaSO_4$) powder was mixed with alginate. In order to achieve the best images, 0.05 g, 0.1 g and 0.15 g of $BaSO_4$ were, respectively, added into 5 ml of 3% (wt/vol) alginate solution (Table 1).

Table 1. Configuration of sample group of physical combination

Sample Name	BS1	BS2	BS3
$BaSO_4$ wt/vol %	1%	2%	3%

A 3D Bio-plotter (envisionTEC Gladbeck, Germany) was employed to fabricate grid patterned alginate scaffolds (Figure 15). The Bio-plotter is a 3-axis, computer-aided manufacturing system which can fabricate 3D scaffolds from various bio-materials. The three alginate/$BaSO_4$ mixtures were dispensed with a 120 micron diameter nozzle under a pressure of 1.0 bar and a temperature of 15℃, while the nozzle was controlled to move horizontally at a speed of 6 mm/s. As the alginate was squeezed through the nozzle into the cross-link medium (50mM calcium chloride plus 50% (vol/vol) glycerol plus 0.1% (wt/vol) poly-ethylenimine), it solidified to form $4\text{ mm} \times 4\text{ mm} \times 4\text{ mm}$ scaffolds. The scaffolds were cross-linked for five minutes and then moved into Dulbecco's Modified Eagle Medium (DMEM).

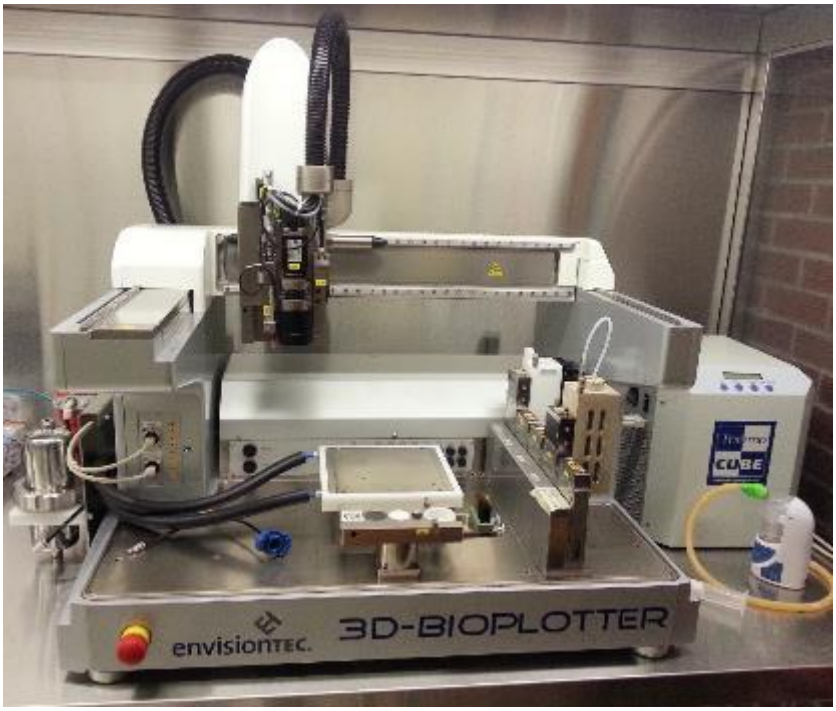

Figure 15. 3D-Bioplotter (envisonTEC) for fabricating alginate scaffolds

2.2.3 Chemical combination of barium and alginate

For the chemical method, barium ions were bonded to alginate molecules during the cross-linking procedure. Alginate can be cross-linked with divalent cations (like Ca^{2+}) in aqueous

solution [63]. Since barium is in the same group with calcium, barium can replace calcium to cross-link alginate (错误!未找到引用源。), meanwhile taking advantages of its contrast enhancement.

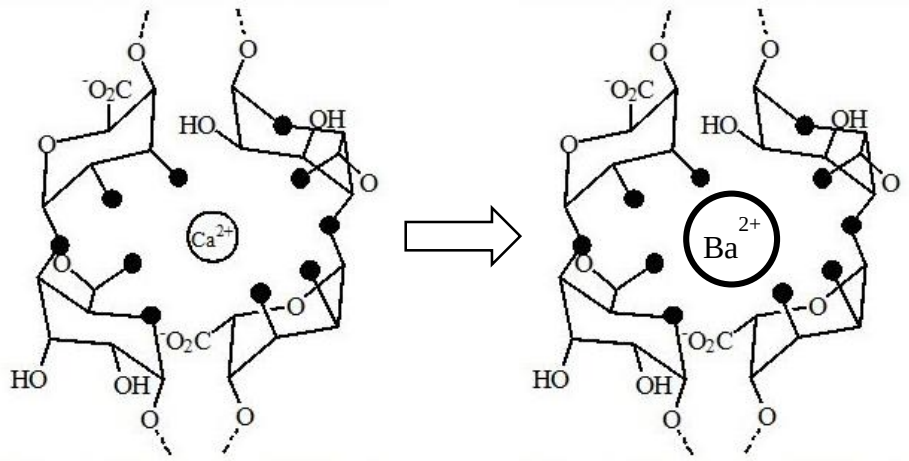

Figure 16. Replace Calcium with Barium to cross-link alginate

A 3% alginate solution was used to fabricate scaffolds by the 3D Bio-plotter at the same settings as the previous one, and three different cross-link media with 30 mM, 50 mM and 100 mM barium chloride plus 50% glycerol plus 0.1% poly-ethylenimine were employed to replace the conventional calcium chloride (Table 2). The scaffolds were cross-linked for five minutes and then moved into the DMEM.

Table 2. Configuration of sample group of chemical combination

Sample Name	BC1	BC2	BC3
Ba^{2+} in cross-link media (mM)	30	50	100

2.2.4 Synchrotron based KES imaging

Synchrotron X-ray imaging was carried out on the Biomedical Imaging and Therapy (BMIT) bend magnet (BM) beamline 05B1-1 at the CLS (Figure 17). BMIT can provide synchrotron-

specific imaging and therapy capabilities. Beamline 05B1-1 allows for either a monochromatic or filtered white beam to be used in the experimental hutch. The monochromatic spectral range spans 8-40 keV. The experimental hutch has a positioning system that allows for the set-up of computed tomography and planar imaging.

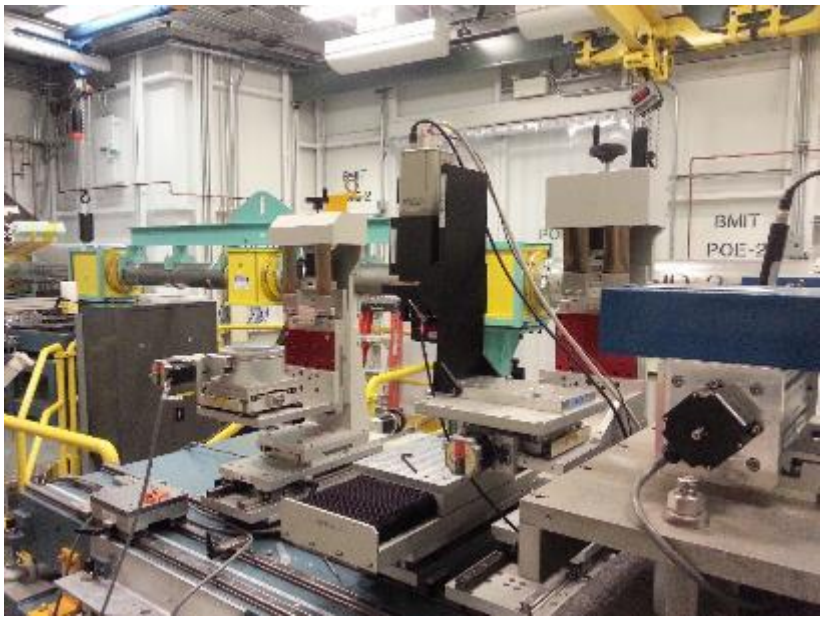

Figure 17. BMIT-BM beamline at the CLS

In this study, the samples were placed in an aqueous solution to simulate a high water content imaging environment. KES imaging was based on absorption imaging at just below and above the energy level of barium's K-edge (37.441 keV). For absorption imaging, the sample-to-detector distance (SD) was set short (2 cm) to reduce phase contrast and attenuation and the detector with a pixel size of 10 micron and a field of view (FV) of 6 mm was chosen. The exposure time for each projection was 0.93 s. The intensity of the images taken at low energy and high energy can be written as

$$I_L = I_0 e^{-\mu_{ML}\rho_M(t-t_C)} e^{-\mu_{CL}\rho_C t_C} \quad (3)$$

$$I_H = I_0 e^{-\mu_{MH}\rho_M(t-t_C)} e^{-\mu_{CH}\rho_C t_C} \quad (4)$$

where I_0 is the original intensity of the X-ray, $\mu_{ML}, \mu_{CL}, \mu_{MH}$, and μ_{CH} are the mass absorption coefficients of the media and the contrast agents at low and high photon energies; ρ_M, and ρ_C are the densities of the media and the contrast agents; t, and t_C are the total thickness and the thickness of the contrast agents. By subtracting the logarithms of (3) and (4) the difference of the logarithmic intensities at low/high energies can be derived as, given for $\mu_{ML} \approx \mu_{MH}$

$$\ln I_L - \ln I_H = (\mu_{CH} - \mu_{CL}) \cdot \rho_C t_C = \Delta\mu_C \cdot \rho_C t_C \quad (5)$$

The image subtraction and the following image processing was completed in the ImageJ software.

2.2.5 Synchrotron-based KES with CT

KES-CT was performed to visualize the inner structure of the scaffolds in 3D from the same beam set-up for all projections. Samples were mounted on a rotary stage and controlled to rotate at a step-angle of $0.12°$ over $180°$ (1500 projections). The number of reconstructed slices can be calculated from

$$\frac{\text{Field of View}}{\text{Pixel Size}} = 600. \quad (6)$$

It is noted that the reconstruction is much more complicated than image subtraction. Thus, in order to reduce calculation, the image subtraction can be pursued before reconstruction so that only one round of reconstruction is required. Raw images were reconstructed by Syrmep Tomo Project using a filtered-back projection (FBP) algorithm. The reconstructed slices were processed by MATLAB R2011b, using threshold removal and histogram equalization for contrast enhancement and noise removal, followed by volume rendering in Avizo 7.0.

2.3 Results

2.3.1 Sample preparation

The scaffolds were fabricated in a cubic shape with a grid pattern as shown in Figure 18, using both physical and chemical methods. The scaffolds with the same barium incorporating method have a similar morphology, thus eliminating the influence of sample variability on the comparison of images.

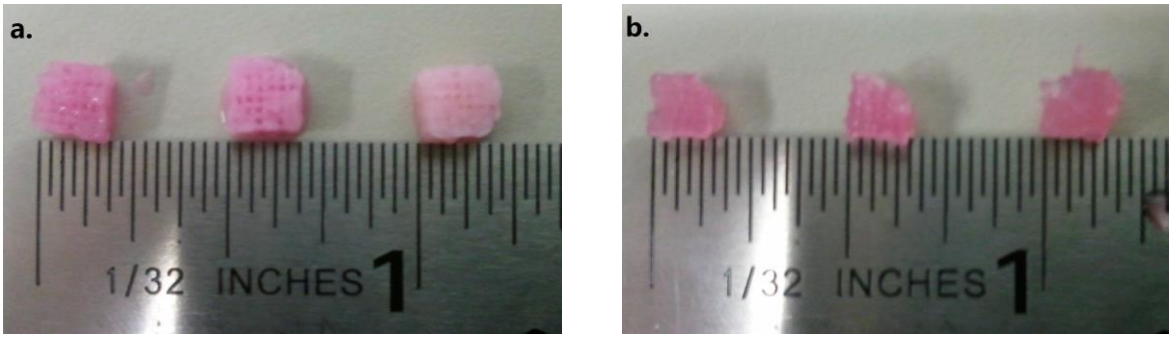

Figure 18. Scaffolds fabricated. (a) Scaffolds marked BS 1~3, (b) scaffolds marked BC 1~3.

2.3.2 KES imaging

Figure 19 shows the photoelectric absorption of barium and hydrogel near 37.441 keV. Compared with conventional radiography (typically applied at photon energy around 10 keV), a much lower dose is inflicted on the scaffolds at this high energy. Unlike conventional radiography which generates contrast from the samples themselves, KES imaging generates contrast from the contrast agent, i.e., barium in this research. According to Figure 19, barium absorbs much more X-rays than hydrogel at a high photon energy like its K-edge for its high atomic number *Z*.

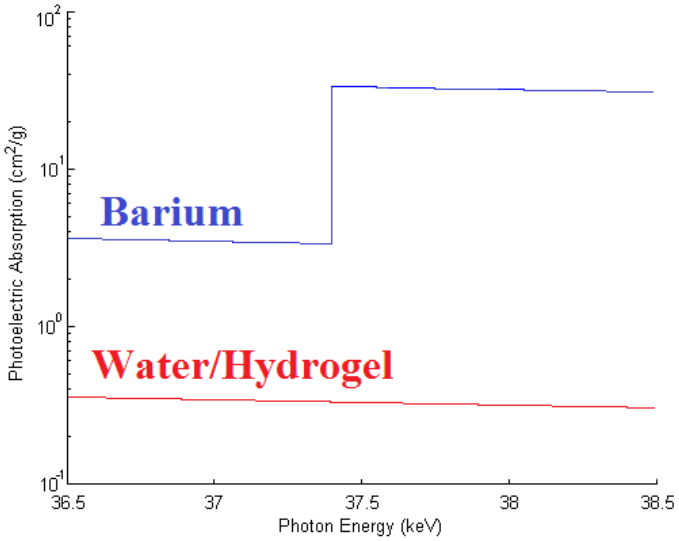

Figure 19. Mass absorption coefficients around barium K-edge (37.441keV)

Images of the alginate/$BaSO_4$ scaffolds are shown in Figure 20. Images in Column 1 were taken at a high energy level above the K-edge of barium, while those in Column 2 were taken at an energy level below the K-edge. Since the X-ray absorption is low at the high photon energy level, the profiles of the scaffolds are hardly visualized via absorption imaging at the energy around the K-edge of barium. The images in Column 1 have stronger contrast than the images in Column 2 since the X-ray absorption boosts at the K-edge. The images in Column 3 were obtained from subtracting the images in Columns 1 and 2. The scaffolds can be identified in the KES images. As the percentage of $BaSO_4$ increases, the contrast of the scaffold increases as well. However, the image of the BS3 scaffold (Figure 20 (c-3)) was not able to provide details such as the grids and strands. The significant black grains in Figure 20 (c-3) indicate that the $BaSO_4$ inside of the scaffold wasn't distributed evenly.

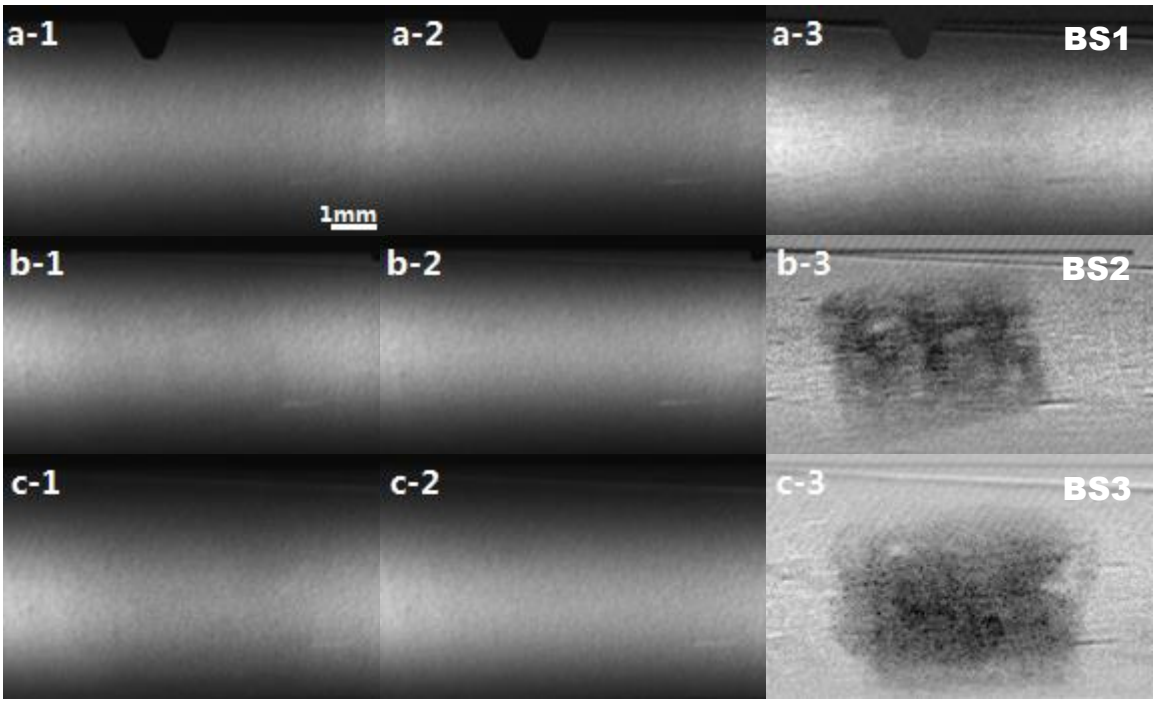

Figure 20. KES images of alginate/$BaSO_4$ scaffolds. (a) BS1 at 37.66keV, 37.33keV, and the image subtraction; (b) BS2 at 37.65keV, 37.36keV, and the image subtraction; (c) BS3 at 37.57keV, 37.40keV, and the image subtraction.

Figure 21 shows the KES images of alginate scaffolds cross-linked in $BaCl_2$ media. Comparing with Figure 20, the images in Columns 1 and 2 have similar characteristics. From the images in Column 3, it is seen that the image quality decreases with concentration of barium ions. Figure 21 (a-3) shows the patterns of the scaffolds, but the contour of the scaffold is not as clear as the one in Figure 20 (b-3).

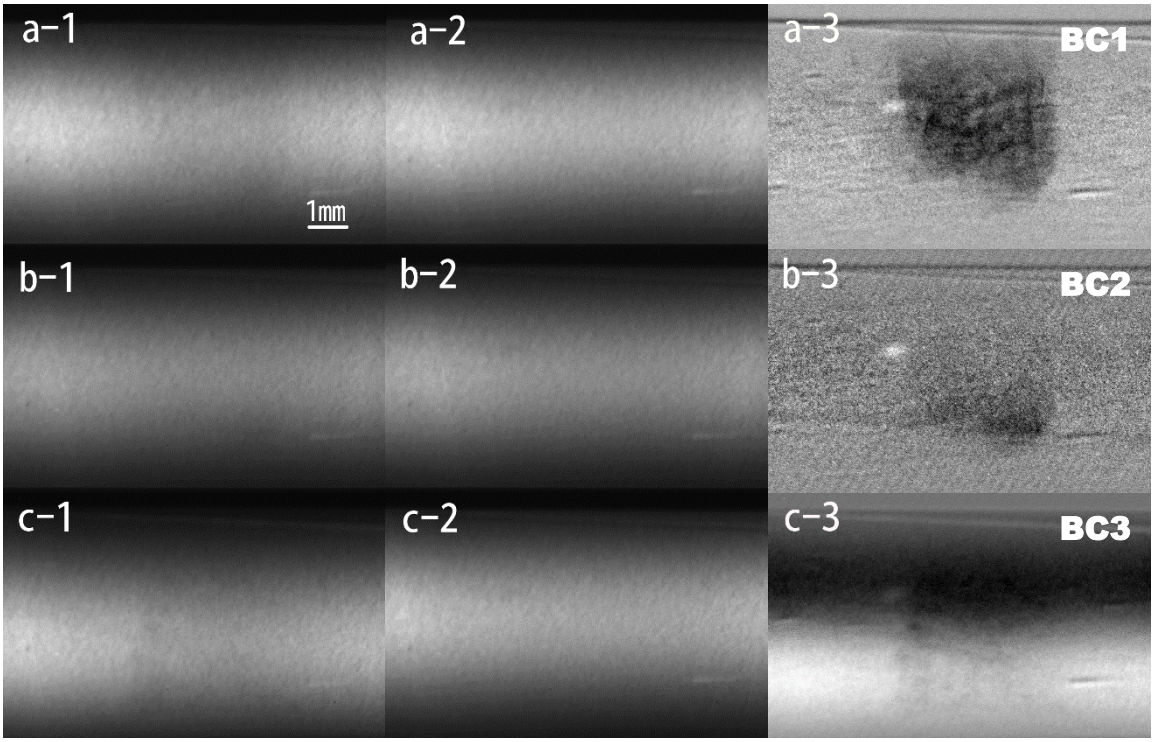

Figure 21. KES images of alginate scaffolds cross-linked by $BaCl_2$. (a) BC1 at 37.58keV, 37.40keV, and the image subtraction; (b) BC2 at 37.65keV, 37.36keV, and the image subtraction; (c) BC3 at 37.65keV, 37.36keV, and the image subtraction.

2.3.3 KES-CT

In order to obtain more detailed information from the KES imaging, computed tomography was applied for the two samples with the best imaging results (BS2 and BC1). Figure 22 shows two slices of the reconstruction from the images of BS2 and BC1. Both slices reveal the detailed pore structures of the scaffold more clearly than projections. The Peak SNR (PSNR) of the two images were calculated as following function:

$$PSNR = 20\log(\text{Peak} - \text{to} - \text{Valley}/\text{standard deviation}) \quad (7)$$

PSNR(a)=16.51dB, *PSNR(b)*=12.68dB. In Figure 22 (a), the image looks dark and the contrast is uniform for the strands. The image in Figure 22 (b) appears to be brighter and has strong contrast at the edges of the strands. The line profile in Figure 22 (c) and (d), which indicate the the grey

values of pixels crossed by the yellow lines in (a) and (b), show the contrast of the scaffolds and the surroundings. Comparing (d) with (c), sharper pitches of the contrast can be found at the edge of the strands, indicating that the chemical method produces higher intensity differences.

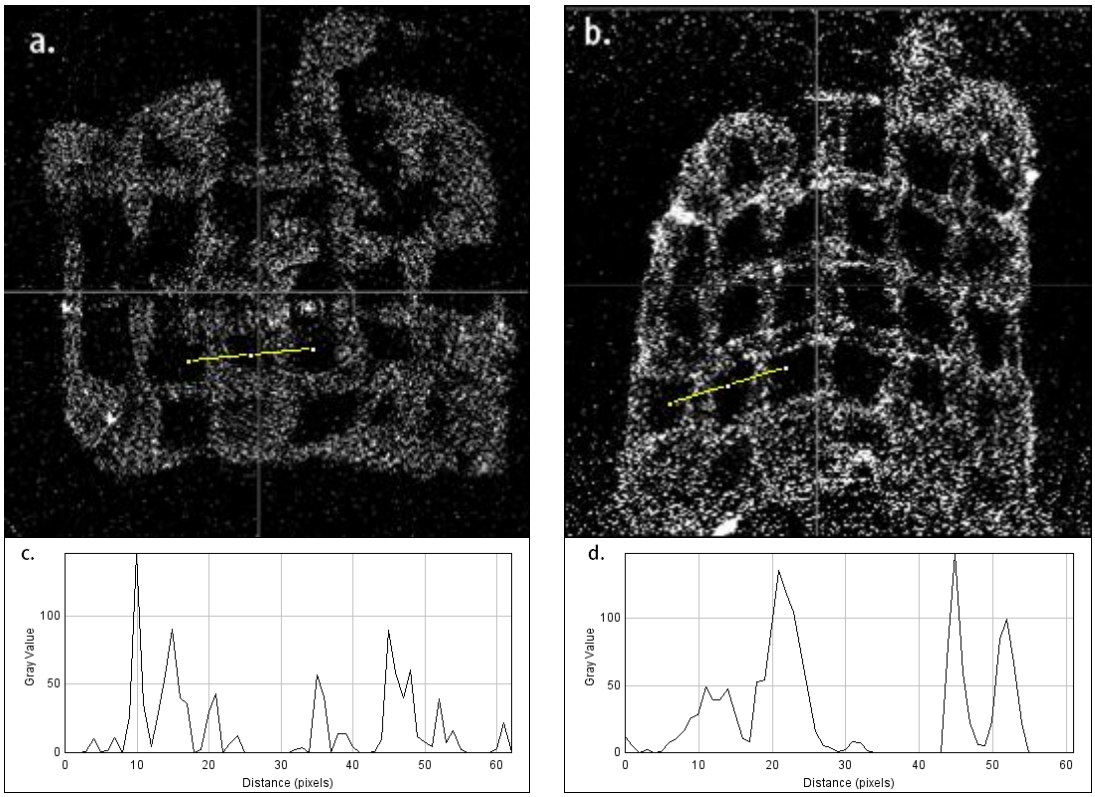

Figure 22. Reconstructed slices of KES-CT. (a) BS2, (b) BC1, (c), (d) are the line profile of gray values corresponding to the yellow lines in (a) and (b), respectively.

For further improvement, image processing methods were applied by using a Gamma transform to enhance the contrast, a median filter to smooth the image, despeckling to reduce noise, and a threshold to remove unnecessary background. Figure 23 shows the rendered volumes of the two images. From these 3D images, the inner structure of the scaffolds is clearly seen. Animations examining the inner structure of the scaffold were also made by Avizo 7.0.

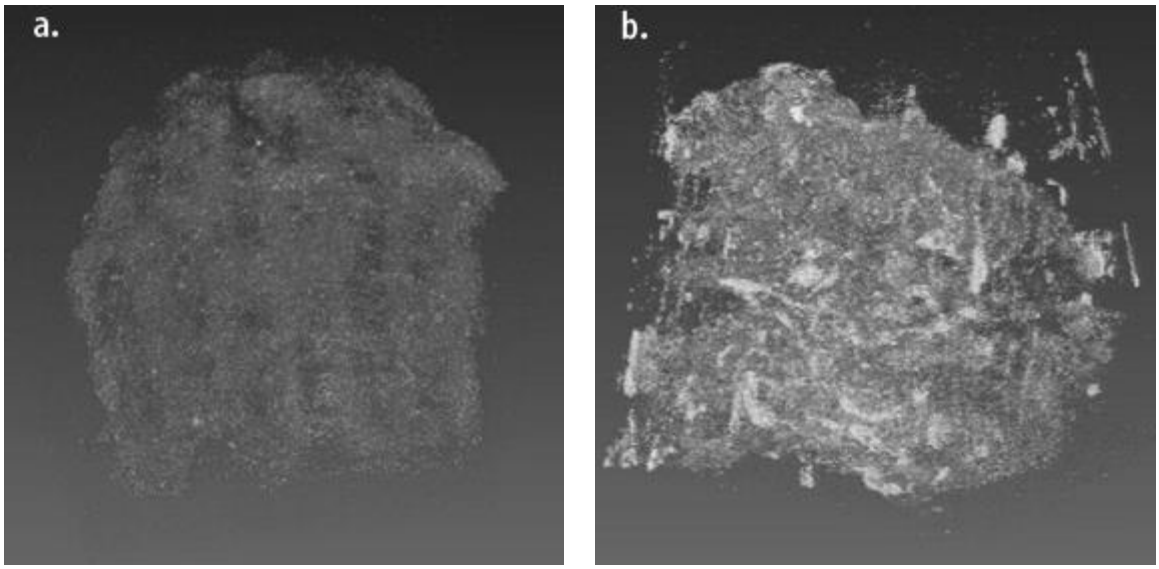

Figure 23. Volume rendering of KES-CT by Avizo. (a) BS2, (b) BC1

2.4 Discussion

This study illustrates a new possibility for using synchrotron-based KES imaging for the visualization of hydrogel scaffolds in high water content environments. Specifically, alginate patterned scaffolds were visualized in an aqueous solution by employing barium as the contrast agent in physical and chemical forms. Both methods were able to reveal feasible images of the alginate scaffolds with identifiable details. Combining with CT, 3D volumes of the scaffolds were obtained and they help to analyze the morphology.

For the alginate/$BaSO_4$ scaffolds, the barium distribution in the scaffolds appears to be grainy as the percentage of $BaSO_4$ increases to a certain level. From the KES scaffold images (3% $BaSO_4$), high contrast of the grains of $BaSO_4$ can be seen. These dark spots may lead to a misunderstanding of the scaffold's structure. On the other hand, a low percentage of $BaSO_4$ cannot produce sufficient contrast to visualize the scaffold. This suggests that the quantity of $BaSO_4$ is important and should be controlled to obtain meaningful images via KES.

Compared to $BaSO_4$, the use of $BaCl_2$ as the cross-linking medium is a new approach, especially for KES imaging of alginate. In the tomography images, the barium cross-linked scaffold has higher contrast and brighter edges. Since the barium ions bonded to the alginate can be distributed more uniformly at a molecular scale, uniform contrast and smooth images are generated. The KES images show that higher concentrations of barium ions lead to poor contrast of scaffolds. One possible reason is that high concentrations of barium ions cross-linked to the surface of the scaffold strands very fast. The dense surface blocks more barium ions from penetrating into the strands so that there isn't enough barium to generate contrast. As such, it is reasoned that the cross-linking time may be an important factor to the KES imaging of scaffolds. This would be an interesting research initiative in the future.

An important concern is the toxicity of the barium cross-linked alginate. Barium ions are considered to be cytotoxic because it is an inhibitor of K^+ channels in bio-membranes at concentrations greater than 5-10 mM [64]. However, high concentration barium cross-linked alginate has been fabricated into micro beads for cell delivery and drug release *in vivo* or *in situ* in some research and has showed significant biocompatibility [65, 66]. One possible explanation is that alginate's affinity toward Ba^{2+} is stronger than Ca^{2+}, which makes Ba^{2+} released *in vivo* unable to reach harmful concentrations. Further experiments are required to test the cell viability in barium cross-linked alginate scaffolds and determine if this method can be applied for *in vivo* imaging.

For X-ray imaging, the higher the energy of the photons applied the lower the dose of X-ray absorbed by the sample. In conventional radiography, absorption dose is usually high since the contrast is mainly contributed by absorption at the low energy level. High image contrast means high dose. In tissue engineering, high X-ray dose is harmful, not only damaging the tissue and

scaffold samples being imagined, but also possibly causing changes in the material properties of scaffolds. Based on absorption imaging, KES is usually performed at high photon energy. The contrast of KES images is caused by the strong absorption of the contrast agents at the K-edge energy where the scaffolds and tissue absorb limited X-rays. Thus KES imaging can be promising for visualization in tissue engineering.

CHAPTER 3
SYNCHROTRON BASED PHASE CONTRAST IMAGING AND TOMOGRAPHY OF ALGINATE SCAFFOLDS WITH CHITOSAN MICRO-SPHERES

3.1 Introduction

Phase contrast imaging (PCI) is based on spatial gradients of the refractive index. In PCI, the distance between the sample and the detector varies from several decimeters to meters, which is longer than the sample – detector distance in the absorption radiography, such that the bending of the beam superimpose at the interface of different structures. This superposition of beam results in the peak and valley of intensity at the edge of sample, which gives higher contrast. Since the X-ray travels further after the sample in PCI, more attenuation of beam will take place. The beams of high flux and brilliance generated by the synchrotron light source are able to maintain the intensity of the images.

Although PCI can visualize soft tissues and low-density materials, it is still difficult to visualize hydrogels in aqueous environments because the refractive index of high-water-content hydrogels differs little from water. If no staining is allowed, markers may be used to enhance the visualization of hydrogel scaffolds. Chitosan, as a biocompatible material, has been widely used in tissue engineering, including serving as a vehicle in the form of microspheres for drug and cell delivery [67, 68]. The chitosan microspheres (CMs) of tens of micron in size can refract X-rays significantly from the matrix of hydrogel and water. On this basis, it is rational to incorporate CMs, as a marker, into hydrogel scaffolds for their visualization in aqueous environment.

In this chapter, alginate hydrogel scaffolds incorporated with CMs were imaged by PCI at the CLS and different amounts of CMs were employed to compare image quality. Tomography was also applied and combined with PCI to obtain 3D profiles of the scaffolds being imagined.

3.2 Materials and methods

3.2.1 Chemicals

Chitosan (28191, Sigma), Span 80, glutaraldehyde (Sigma), and acetic acid (Fluka) were used to fabricate chitosan microspheres; and alginate, calcium chloride, glycerol, and PEI (the same with Chapter 2, Sigma) were used to fabricate the scaffolds.

3.2.2 Preparation of chitosan micro-spheres

CMs were prepared using an emulsion-ionic cross-linking method [69]. 200 mg of chitosan was dissolved in 10 mL of 1% (wt/vol) acetic acid solution to form the water phase. 1 mL of Span 80 was dropped into 50 mL of paraffin oil using a magnetic stirrer at a speed of 1000 rpm to form the oil phase. The water phase was then dispersed into the oil phase and stirred for 30 minutes to form water-in-oil (W/O) emulsion. Next, 1 mL of glutaraldehyde was slowly dispersed in the W/O emulsion to cross-link the chitosan droplets. After 2 hours of cross-linking, the CMs were solidified and then washed two times with propanol, two times with ethanol, two times with distilled water, and eventually separated by means of centrifugation at 3000 rpm. The final product was obtained by cryochem.

3.2.3 Fabrication of alginate scaffolds with CMs

0.05 g, 0.1 g and 0.15 g of CMs were, respectively, mixed with 5 mL of alginate solution. Considering the particles' flow in the nozzle, the samples' size was designed larger as $5\ \text{mm} \times 5\ \text{mm} \times 5\ \text{mm}$. The grid-patterned scaffolds were fabricated with 1%, 2% and 3% CMs (denoted by CM 1~3) by a 3D Bio-plotter. For scaffold fabrication, the mixture was dispensed via a 200 micron diameter nozzle under an operating pressure of 1.5 bar, a temperature of 20℃, and a horizontal nozzle speed of 15 mm/s. The alginate was squeezed through the nozzle into the cross-link medium (50 mM calcium chloride plus 50% (vol/vol) glycerol plus 0.1% (wt/vol) poly-

ethylenimine). The scaffolds were cross-linked for five minutes and then moved into the Tris buffer.

3.2.4 Synchrotron based in-line PCI

Synchrotron X-ray imaging was performed on the BMIT-BM beamline 05B1-1 at the CLS. The samples were placed in an aqueous solution in order to simulate the high-water-content imaging environment *in vivo*. The in-line PCI was performed at 20 keV. The SD was set as 110 cm for the best phase contrast. The exposure time for each projection was 0.9 s. The detector was chosen with a pixel size of 10 micron and field of view of 6 mm. All images were then processed in ImageJ.

3.2.5 In-line PCI-CT

In-line PCI-CT was performed to visualize the 3D structure of the scaffolds. The beam was set the same for all projections. Samples were mounted on a rotary stage, which rotated at a step-angle of 0.12 °over 180 °(1500 projections). Raw images were reconstructed using Syrmep Tomo Project with FBP algorithm. The reconstructed slices were processed by MATLAB R2011b for contrast enhancement and noise removal, followed by the volume rendering in Avizo 7.0.

3.3 Results

3.3.1 Sample preparation

The cubic scaffolds were designed with a grid pattern and fabricated using a dispensing rapid prototyping method. However, the addition of CMs negatively affected the fabrication of the alginate scaffolds, sometimes resulting in discontinuous dispensing of material (this needs to be addressed in the future). As a result, the scaffolds fabricated do not have the designed shape, as shown in Figure 24. However, the visualization results still provide worthy guideline to further study.

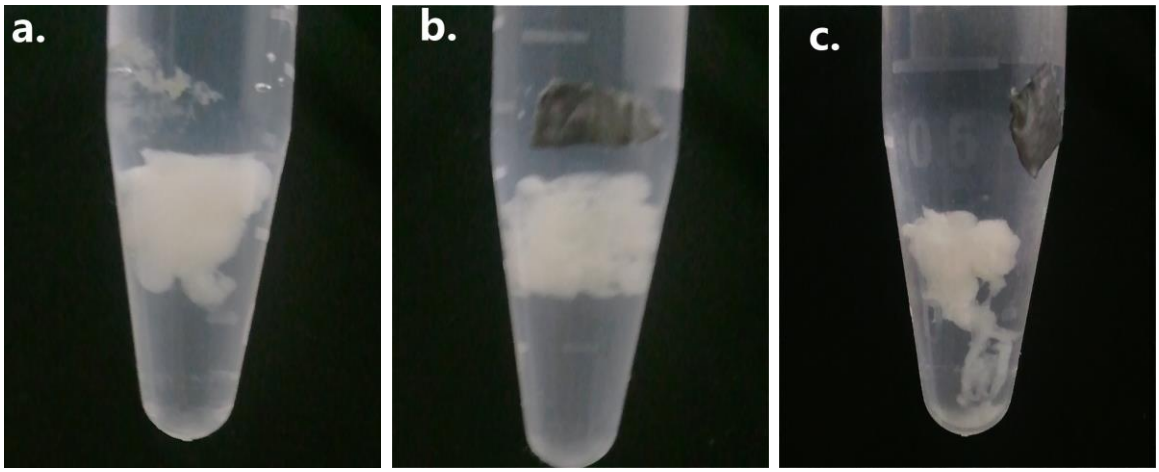

Figure 24. Alginate scaffolds with CMs. (a) CM1, (b) CM2, (c) CM3

3.3.2 In-line PCI

Figure 25 shows the in-line PCI of alginate/CMs scaffolds. In all three images the profile of the scaffolds formed with clusters of spots can be identified. As the percentage of the CMs increases, the scaffolds become more visible in the images. However, it is also observed that all the raw images suffered insufficient contrast even when the histograms of the images were equalized.

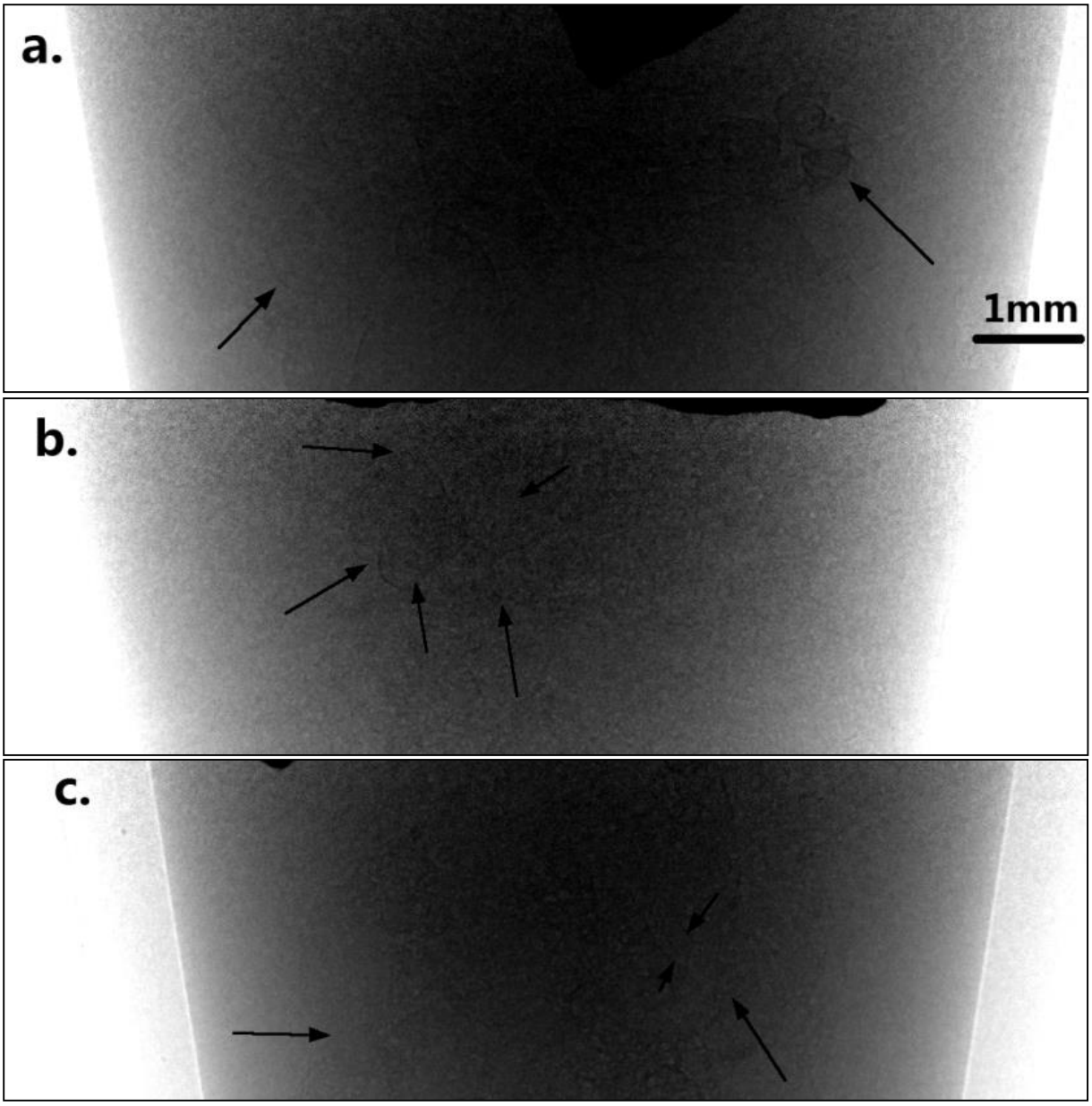

Figure 25. In-line PCI of alginate/CMs scaffolds, black arrows point to clusters of dark spots which indicate the CMs. (a)~(c), CM1~3

3.3.3 In-line PCI-CT

Computed tomography was employed to generate 3D images from the projections of the sample. Figure 26 shows the reconstructed slice and rendered volume of in-line PCI-CT of CM3. The PSNR of this slice image were: *PSNR*=27.9dB, which indicated that the PCI-CT image performed better quality than KES-CT image. In Figure 26(a), the CT slice revealed both CMs and the contour

of the scaffold, which performed more information than the projection images. The peak-valley in the two red circle rings in Figure 26(c) indicated the significant contrast edge of the alginate scaffold and media. In Figure 26(a), the edge of alginate scaffold was clear enough to identify, suggesting there is still a spatial gradient of the refractive index at the interface of the alginate hydrogel and water environment. The significant trough in the red ellipse ring revealed the location of CM, and suggested the large difference in the refractive indices and densities between chitosan and alginate. Since the percentage of CMs incorporated was limited, the distribution of CMs is observed, but not enough to represent the profile of the scaffolds.

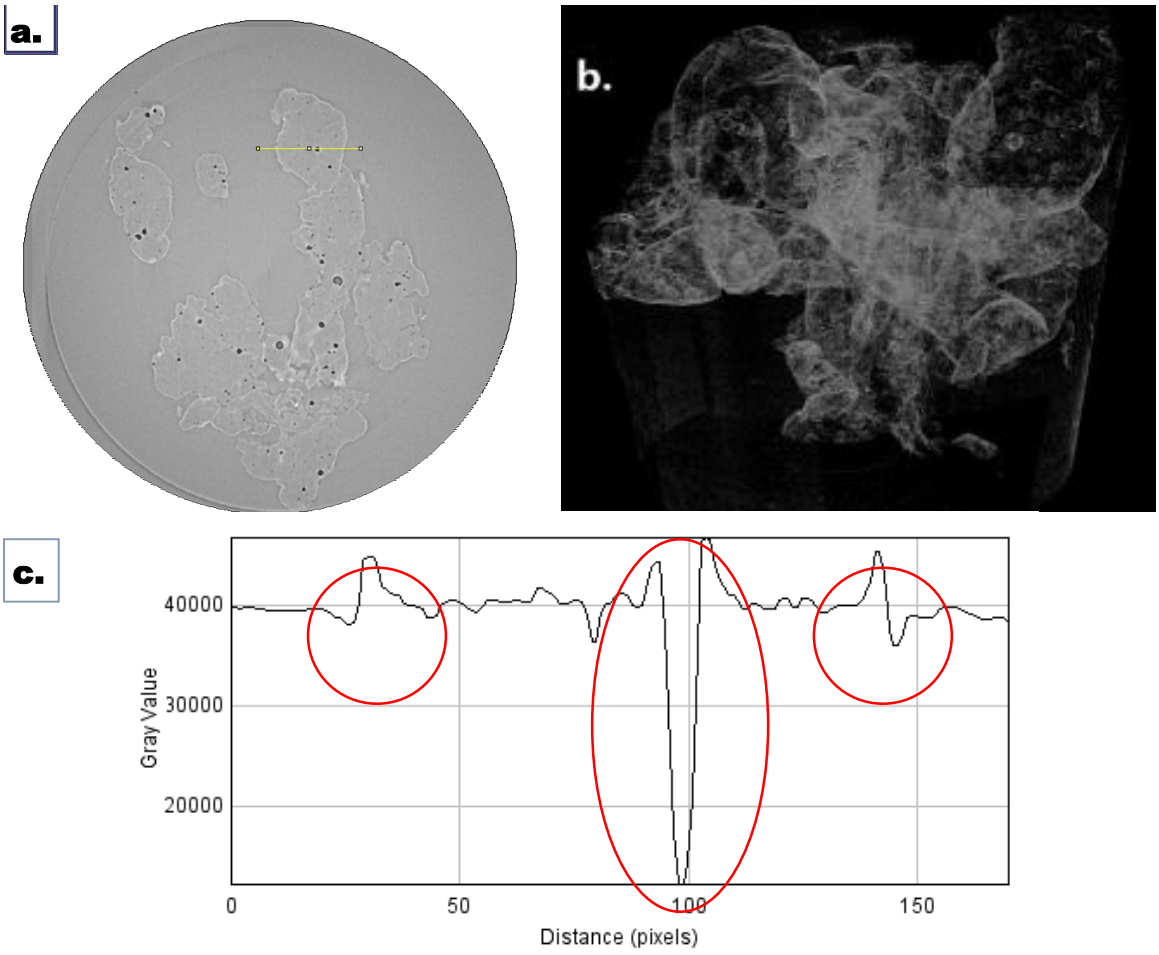

Figure 26. (a) CT reconstructed slice of alginate scaffold with CMs, (b) rendered volume, and (c) line profile of gray value corresponding to the yellow lines in (a) (CM3)

3.4 Discussion

This chapter presents a preliminary study of hydrogel scaffold visualization in aqueous environments based on synchrotron-based phase contrast imaging with the help of high-density particles as a contrast agent. Specifically, CMs were incorporated in alginate scaffolds, which were then visualized by means of in-line PCI and CT. The results illustrate that the projections of in-line PCI produce limited visibility of the scaffolds and CMs. However, the reconstructed CT is able to provide clearer images.

For an alginate hydrogel scaffold, the high water content results in little difference in density between the aqueous environment and the scaffold leading to limited contrast in PCI. Materials with high density, such as chitosan, can improve the contrast in PCI. In this chapter, the CMs were incorporated and to help identify the morphology of the scaffold being imagined. The PCI in Figure 25 shows limited visibility of CMs and scaffolds. With the introduction of CT, Figure 26 illustrates that CT is able to not only generate 3D image from the projections, but also provide improved contrast of the images. The visibility of CMs in Figure 26 also suggests a means to study CMs that has been widely applied in tissue engineering for cell and drug delivery.

Figure 26 indicates that the profile of the scaffold was not able to be identified from the distribution of CMs due to their low concentration in the scaffold. The increase in the concentration of CMs would improve the scaffold images but their negative effect on the scaffold fabrication (i.e., the discontinuous dispensing of materials as mentioned previously) needs to be addressed in the future.

CHAPTER 4
SYNCHROTRON-BASED PHASE-CONTRAST IMAGING AND TOMOGRAPHY OF ALGINATE SCAFFOLDS WITH GOLD LABELED CELLS

4.1 Introduction

Synchrotron radiation can generate X-rays of high flux and brilliance, which can be applied to produce much better images than conventional X-ray sources. Different from conventional X-ray sources that are generated from one point, the synchrotron light source has parallel beams, which make it possible for the object is to be imaged at the same scale regardless of the change in the sample-to-detector distance (Figure 27).

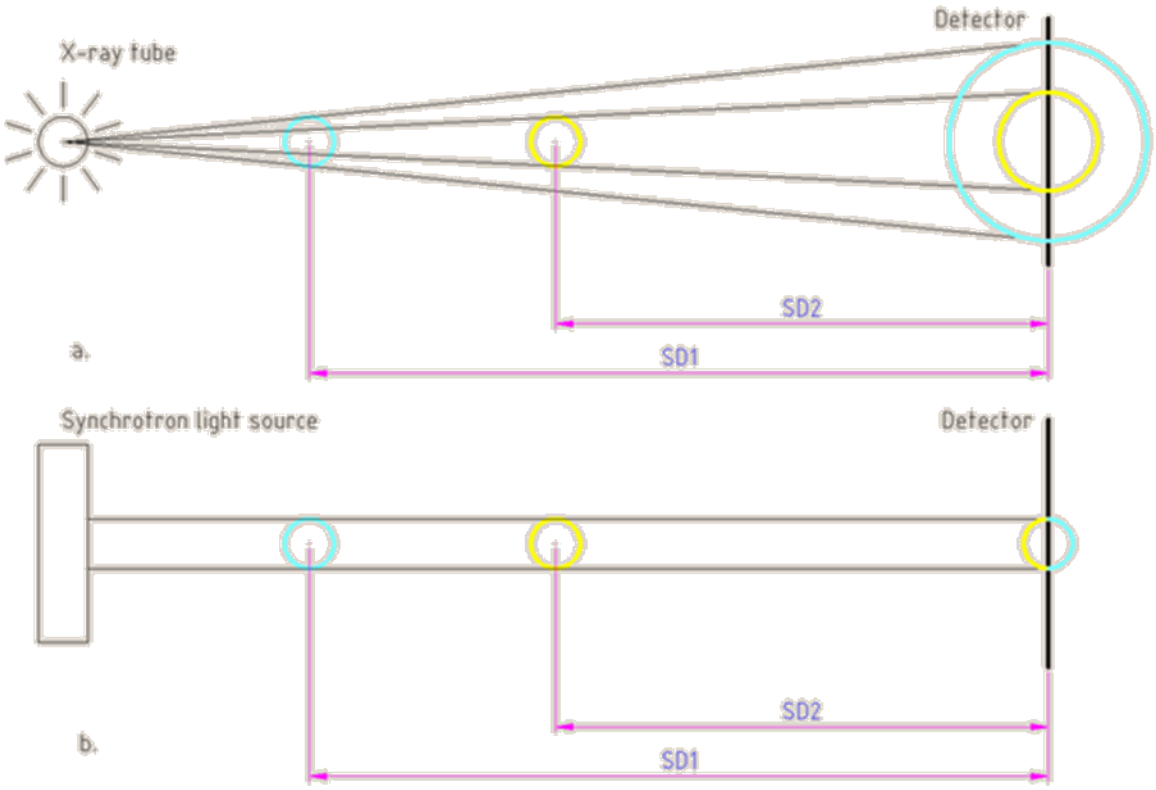

Figure 27. Schematic diagrams of imaging using different light sources: (a) conventional X-ray tube, (b) synchrotron light source

It has been recognized that cells are difficult to visualize using synchrotron imaging methods due to their high water content. One method for improvement is to use a marking agent [57] and for this, gold has shown promise due to its cyto-compatibility and strong X-ray absorption [58-60].

As shown in Chapter 3, alginate scaffolds can be visualized in aqueous solution by PCI-CT. On this basis, this chapter presents an extended study on the visualization of the alginate scaffolds that are encapsulated with cells. Specifically, cells were marked with gold nano-particles (GNPs) to enhance the contrast in absorption radiography, and the alginate scaffolds were cross-linked with different schemes, i.e., varying the cross-linking time and cross-linker concentrations for improved PCI results. Eventually, tomography was also applied to reconstruct the 3D shapes of the scaffolds.

4.2 Materials and methods

4.2.1 Chemicals

Gold (III) chloride trihydrate ($HAuCl_4 \cdot 3H_2O$), sodium citrate tribasic dihydrate, potassium carbonate and polyethylene glycol (Sigma) were used to prepare gold nano-particles. DMEM, horse serum, fetal bovine serum (FBS), phosphate buffered saline (PBS) and trypsin were used to culture and collect cells. Alginate, calcium chloride, glycerol, PEI, (the same with Chapter 2, Sigma) was used to fabricate the scaffolds.

4.2.2 Preparation of GNPs and label serum proteins

GNPs of approximately 50 nm were prepared according to the procedure reported in [70]. Briefly. 1 mL of 1% $HAuCl_4$ solution was added to 100 mL of distilled water, which was then mixed with 2 mL of 1% tri-sodium citrate. The mixture was boiled under reflux for 15-30 minutes until the color became wine red. After cooling down, 0.5 mL of 0.1 M K_2CO_3 was added to make the pH value between 5 and 6, which was roughly measured by pH paper.

To label the serum proteins with GNPs, 1 mL of horse serum was added into the gold solution and 5 minutes later, 0.3 mL of 5% polyethylene glycol was added, with gentle stirring to ensure

the GNPs were evenly distributed in the solution. Then, the colloidal gold was pelleted by centrifugation at 15,000 g for 45 minutes. The supernatant was removed without disturbing the pellet. The tubes were refilled with PBS in which the pellet was resuspended and centrifuged again as described above. After removing the supernatant, the second pellet was resuspended in 10 mL of DMEM plus 10% fetal bovine serum FBS [71].

4.2.3 Cell culture with GNPs

The rat Schwann cell line (RSC96, ATCC) was cultured in the DMEM plus 10% FBS and GNPs-labeled serum at 37 ℃ under 5% carbon dioxide in incubator for 72 h. The cell monolayer on the culture dish was rinsed with PBS and cleaved by trypsin. The cells were then suspended in 5 mL of DMEM and centrifuged at 800 rpm. One control group of cell samples is cultured in DMEM plus 10% FBS.

4.2.4 Fabrication of scaffolds with cells

The supernatant media of cell suspension was subsequently removed and the cells were resuspended in 3 mL of DMEM plus 10% FBS, then mixed with 3ml of 6% alginate to make the final 3% alginate with cells. A 3D Bio-plotter was used to fabricate patterned scaffolds with the alginate (approximate 2×10^7 cells/mL) under a pressure of 1.0 bar. A 120 micron nozzle was used for dispensing the alginate mixture at a temperature of 15℃ and a moving speed of 6 mm/s, into the cross-link media, forming scaffolds in a grid pattern with an overall size of $4\,\text{mm} \times 4\,\text{mm} \times 4\,\text{mm}$. The scaffolds were cross-linked in media of 30 mM, 50 mM and 100 mM calcium chloride (plus 50% glycerol plus 0.1% poly-ethylenimine), respectively, for 5 minutes. Then the samples were moved into DMEM and this group of samples were referred to as Group C (concentration). Another group were set to test the influence of cross-linking duration (Group T) on the quality of images. In Group T, the scaffolds were fabricated with normal 3% alginate and cross-linked in the same media (50 mM calcium chloride plus 50% glycerol plus 0.1% poly-

ethylenimine) for 5 minutes, 30 minutes and 1 hour, respectively (Table 3)Table 1. All the scaffolds were then kept in Tris buffer.

Table 3. Configuration of samples with different cross-link strategies

Sample Name	Concentration			Time		
	C1	C2	C3	T1	T2	T3
Ca^{2+} in Cross-link media (mM)	30	50	100	50		
Cross-link Time (min)	5			5	30	60

4.2.5 Synchrotron imaging

Synchrotron X-ray imaging was carried out on the BMIT-BM beamline 05B1-1, at the CLS. In this experiment, projections were taken using absorption imaging for visualizing the GNPs-labeled cells and in-line PCI for the alginate scaffolds. The samples were placed in an aqueous solution in order to simulate a high water-content imaging environment. For absorption imaging, the SD was set short (10 cm) to reduce phase contrast and attenuation. The energy level for absorption imaging was chosen relatively low at 16 keV to increase absorption. In-line PCI was performed at relatively high energy level (20keV) and long SD (110 cm) to enhance phase contrast and reduce absorption and attenuation. Due to the parallel beam from the synchrotron source (Figure 27), the absorption images and the phase contrast images of the same sample can be readily merged without additional adjustment (Figure 28). The exposure time for each projection was set as 1 s and a detector of 4 micron pixel size was used. The field of view was 6 mm and all images obtained were processed in ImageJ.

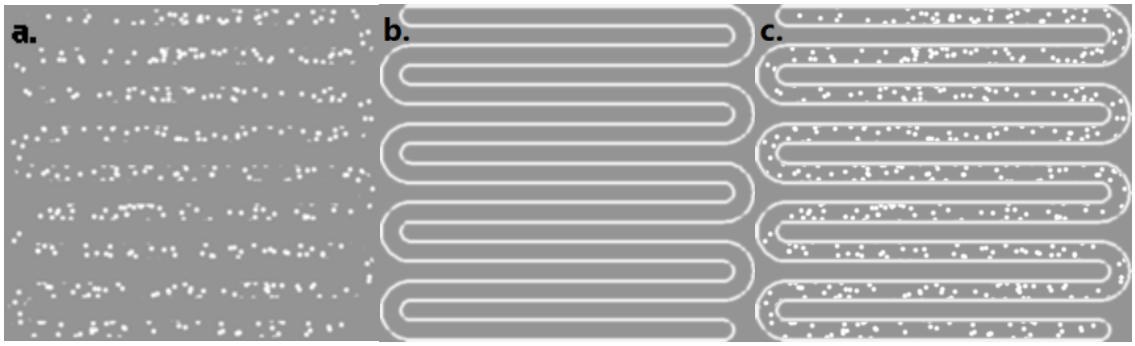

Figure 28. Synchrotron images: (a) absorption image, (b) in-line PCI, (c) merged image

4.2.6 Synchrotron-based imaging with tomography

Synchrotron-based CT was carried out to visualize the inner structure of 3D scaffolds. The beam was set up the same as for the single projections. Samples were placed on a rotary stage with a step-angle of 0.12° over 180° (1500 projections). Raw images were reconstructed using Syrmep Tomo Project with FBP algorithm. The reconstructed slices were processed in MATLAB R2011b and then volume rendered in Avizo 7.0.

4.3 Results

4.3.1 Sample preparation

The appearance of the GNPs labeled cells and normal cells after centrifugation are shown in Figure 29. The cells labeled with GNPs appear black, the same color as the GNPs.

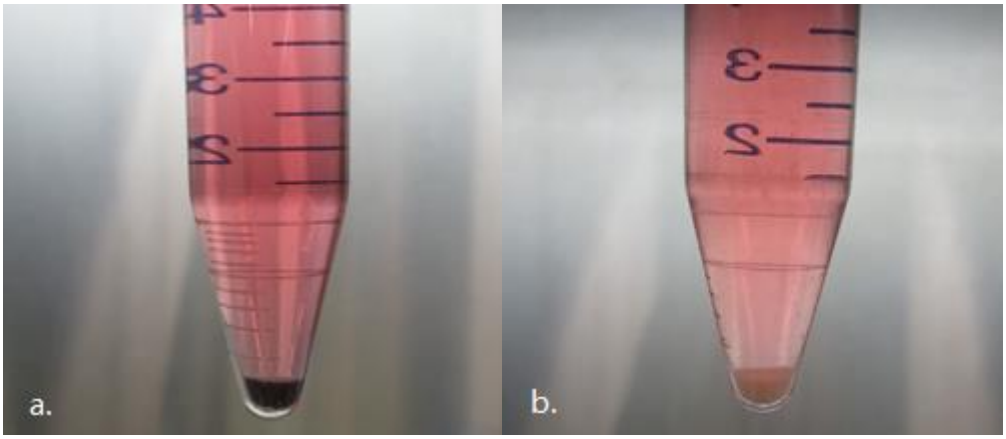

Figure 29. Appearance of centrifuged cells: (a) GNPs labeled cells, (b) normal cells

The scaffolds were fabricated with a grid pattern by using a dispensing-based rapid prototyping method. As shown in Figure 30, the scaffolds in the same group have similar morphology, thus eliminating the influence of sample variability on the comparison of images.

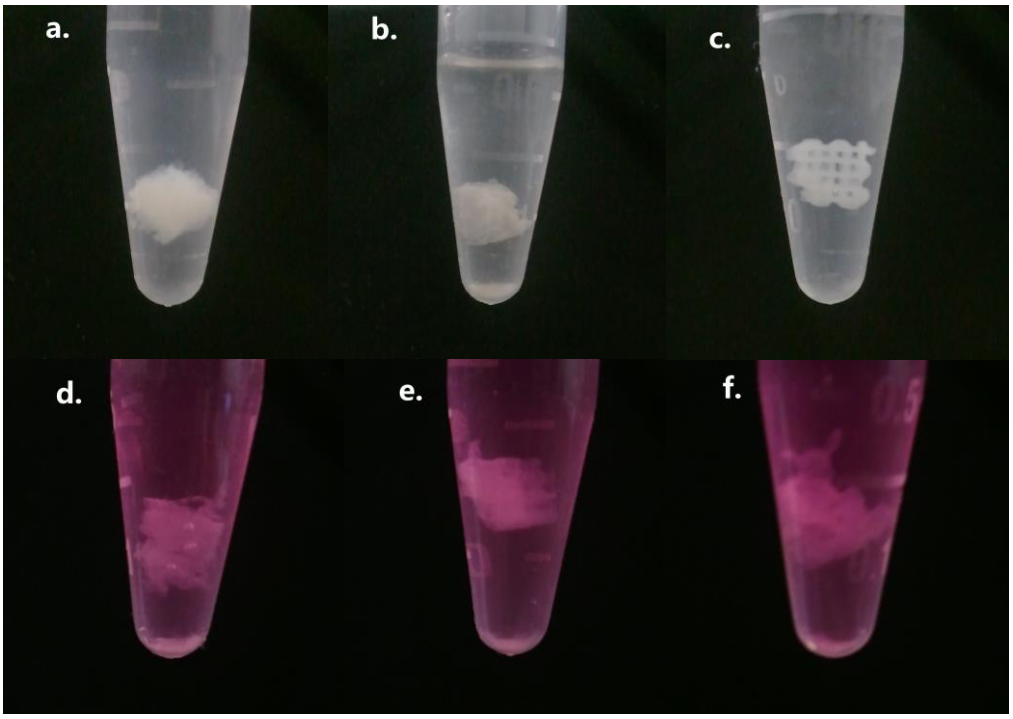

Figure 30. Alginate scaffolds in Tris buffer. (a)~(c), T1~T3; (d)~(e), C1~C3

4.3.2 Absorption imaging for GNPs labeled cells

Absorption radiography was applied for Group C samples. As Figure 31 shows, there is no identifiable feature of the scaffolds but some blurred dark spots exist. The alginate scaffolds could not be visualized using absorption radiography. On the other hand, the dark spots (indicated by the white arrows) may indicate the GNPs labeled cells because of the strong X-ray absorption of the gold. However, since the photons were absorbed by limited GNPs, the SNP was relatively low [67]. Appreciable noise in the image might interfere with the identification of the labeled cells. This needs to be addressed in the future in order for the proposed CT to become feasible for imaging the GNPs labeled cells.

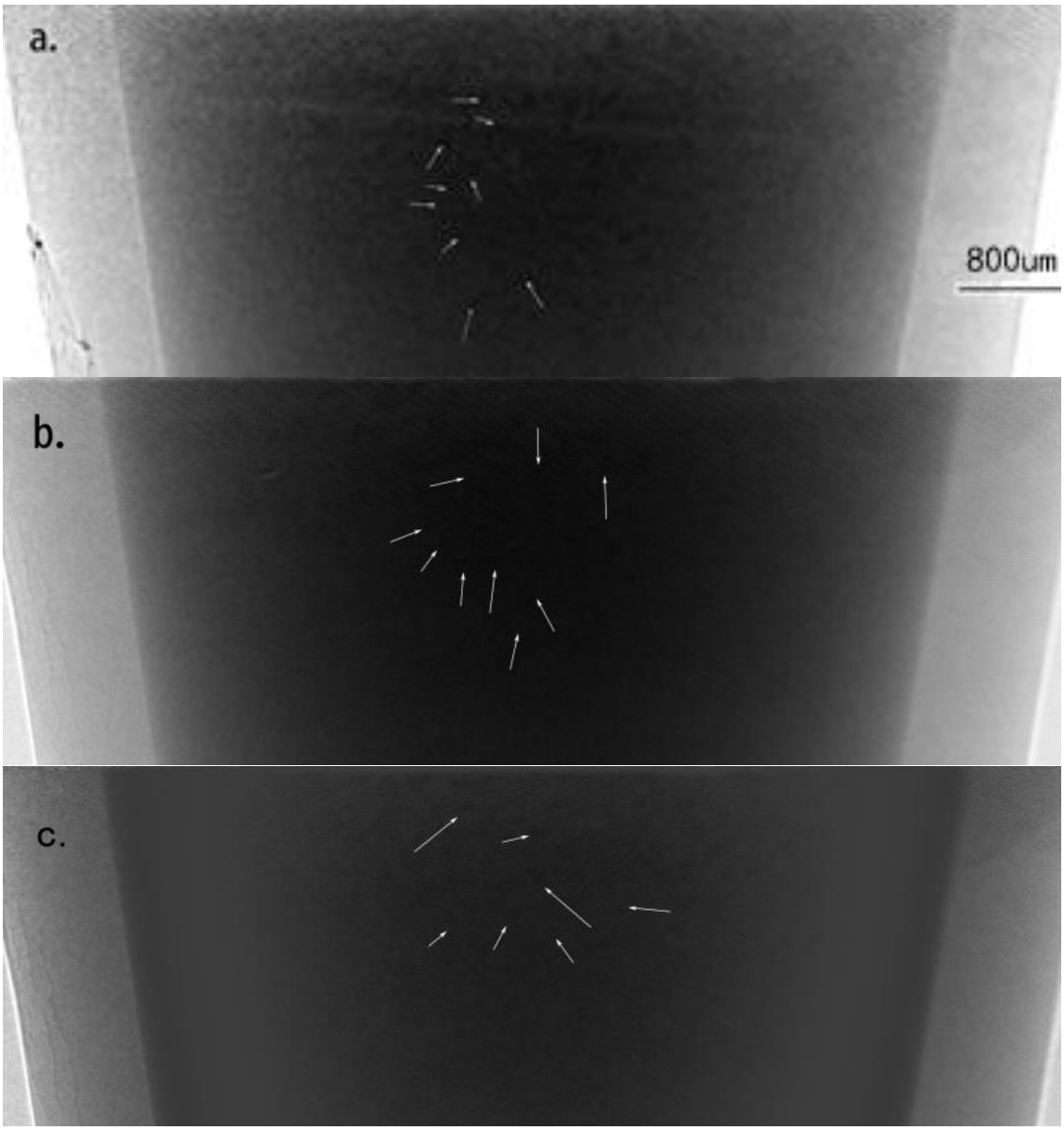

Figure 31. Absorption images of scaffolds with GNPs labeled cells, white arrows point to dark spots which may indicate the labeled cells. (a)~(c), C1~C3

4.3.3 PCI for alginate scaffolds

The PCI for alginate scaffolds presented here was performed with a detector of 10 micron in order to increase the number of photons absorbed per pixel and improve the images. Figure 32 shows the in-line PCI of samples of Group C and Group T. The images of Group C reveal a few

identifiable features of the scaffolds but not the detailed structure (two dark bars of similar shape in Figure 32 (b) and (c) can be considered as the defect of the detector). As the concentration of the cross-link media increased, the contrast didn't change much. In Group T, the contrast of images enhanced as the time of cross-link increased. The longer the alginate was cross-linked, the more the scaffold was solidified, and the gradient of its refractive index was larger. In Figure 32 (f), the multi-layered structure of scaffolds can be recognized.

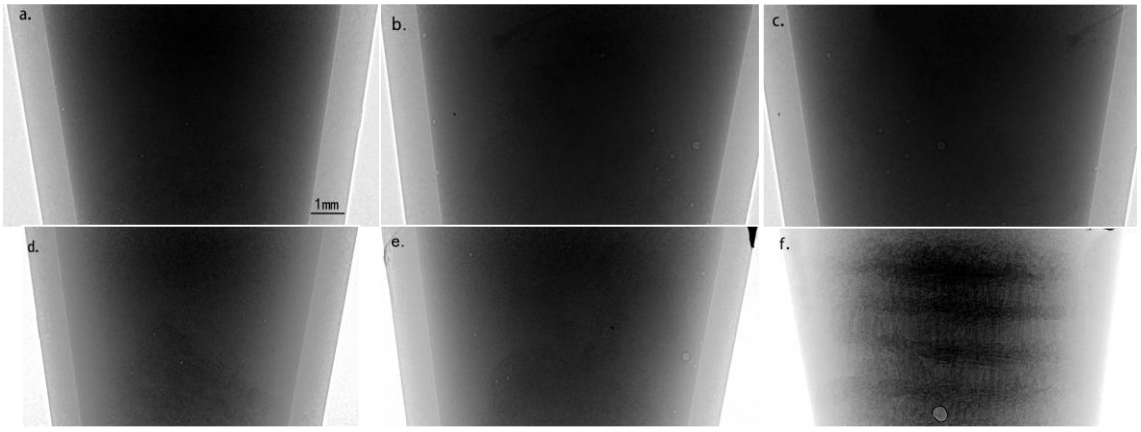

Figure 32. PCI of scaffolds at different cross-link levels. (a)~(c), C1~C3; (d)~(f), T1~T3

4.3.4 In-line PCI-CT

In order to obtain 3D information of the scaffold, CT was applied for the T3 sample. Figure 33 shows one slice from the reconstruction and rendered volume. The PSNR of this slice image were: *PSNR*=22.4dB. According to Figure 33 (a), the inner structure of the scaffold was clearly visualized with high contrast, especially highlighting the interface of the scaffold and the medium. With the rendered volume profile shown in Figure 33 (b), the structure of any cross section can be obtained by examining the different depths of the sample. The line profile in Figure 33 (c) revealed the multiple layers of the sample by steady periodic peak-trough differences.

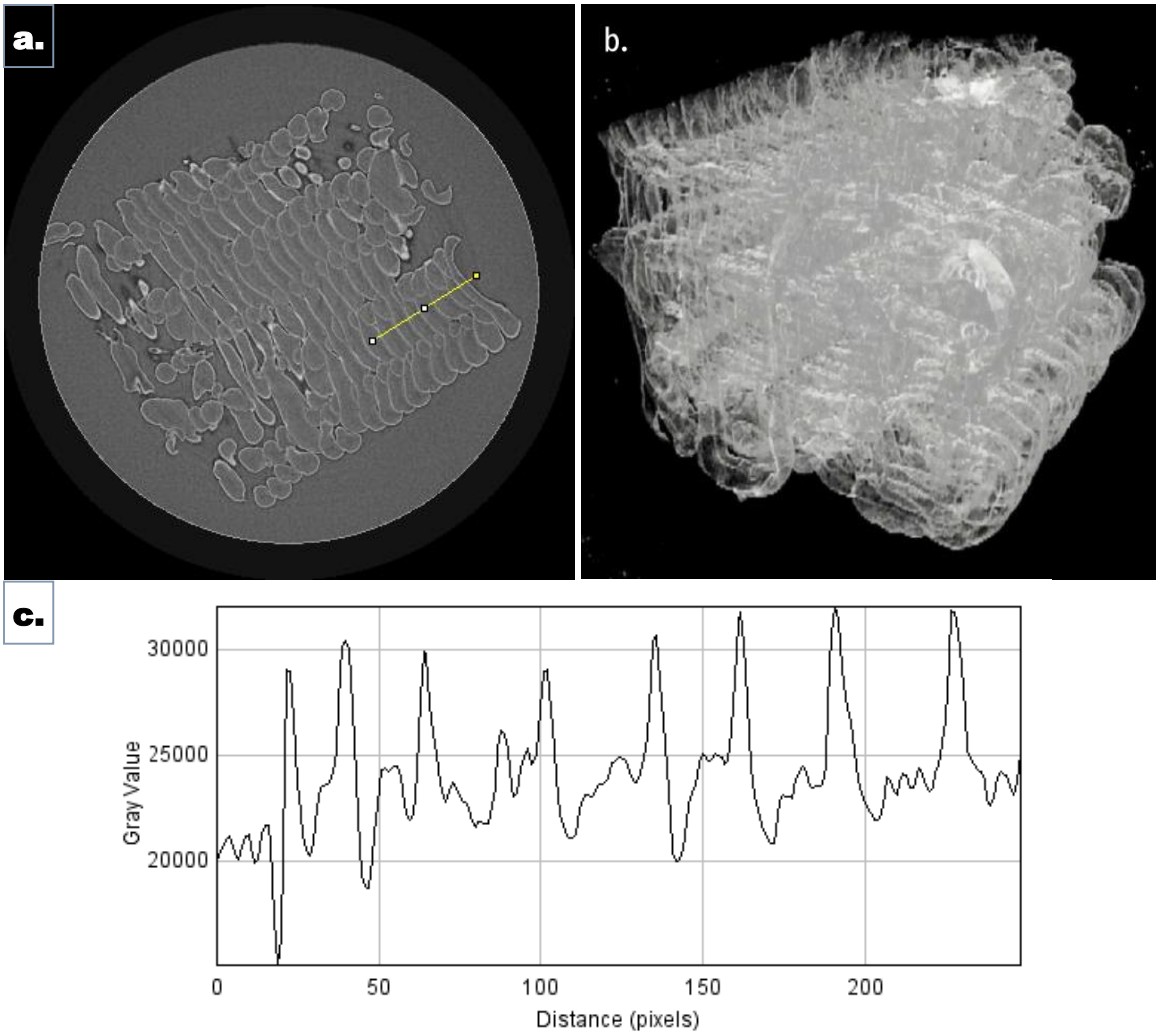

Figure 33. (a) in-line PCI-CT reconstructed slice of alginate scaffold, (b) rendered volume, and (c) line profile of gray value corresponding to the yellow lines in (a) (T3)

4.4 Discussion

The goal of this study is to visualize hydrogel scaffolds encapsulating living cells in aqueous environments by synchrotron-based radiography and phase-contrast imaging. Specifically, GNPs were introduced to label cells to generate contrast by absorption radiography and in-line PCI and CT were applied to visualize the alginate scaffolds and cells. The images of the GNPs labeled cells showed preliminary results of cell distribution and the results of in-line PCI of the scaffold

illustrated that the visibility of alginate scaffolds by in-line PCI could be affected by the cross-link time.

In the present study, cells can hardly be visualized simply using synchrotron imaging methods, but there is potential to take advantage of the strong absorption property of noble metals such as gold for their visualization. The dark spots appearing in Figure 31 can be a positive preliminary result of this idea. The contrast of those spots is not strong enough to distinguish the labeled cells from noise or defects in the detector. It is suggested that a higher concentration of GNPs be applied for enhanced contrast in the future. On the other hand, absorption edge subtraction can be applied to enhance the contrast of gold, as mentioned Chapter 4. The K-edge of gold is 80.725 keV, at which the photoelectric absorption is quite low even if there is a boost at the edge. Instead of the K-edge, the L-edge of gold (14.353 keV) can be applied for imaging. By subtracting the images taken above and below the L-edge, unnecessary background information will be removed, thus enhancing the contrast. With the aforementioned methods, the visualization of cells may become feasible, thus being able to achieve 3D images of cells by means of the CT technique.

According to the result of in-line PCI, the visibility of the alginate scaffolds depends on the cross-link time of the material. On the other hand, the concentration of the cross-link medium didn’t make a significant difference in the imaging results. The main cause of the different imaging contrast is the cross-linking time. One hour of cross-linking in 50 mM calcium solution has been confirmed to produce significant contrast. Future studies should focus on the quantitative relations between the cross-link level and the refractive index of the cross-linked alginate. Better control of the cross-linking can help to improve the visualization of the scaffolds as well as the cell viability.

CHAPTER 5
CONCLUSION, DISCUSSION AND FUTURE WORK

5.1 Conclusions and Discussion

Three methods based on synchrotron techniques were performed for scaffold imaging in this study. Alginate scaffolds were imaged by KES and in-line PCI with different contrast agents. From this study, the following conclusions can be drawn.

Non-invasive and high resolution visualization of hydrogel scaffolds in aqueous environment is challenging. With the help of barium that was incorporated in the scaffolds by either physical or chemical means, KES images of the alginate scaffolds were able to demonstrate enhanced contrast of the scaffolds. Compared with traditional method of mixing $BaSO_4$, barium cross-linked alginate can be visualized more clearly with higher quality. Combined with tomography, the KES images can show the detailed microstructure of the scaffolds which can be used for analysis and further design. This technique provides feasible images with a low dose at high photon energy. KES imaging shows great potential for visualization of alginate scaffolds in high water content environments.

Phase-contrast imaging has great potential to visualize soft tissues and materials by generating contrast from the difference of the densities. Taking advantage of the higher density, chitosan micro-spheres were introduced as a contrast agent to enhance the scaffold images. Since a small amount of CMs cannot distribute effectively in the scaffolds, they can hardly generate sufficient contrast to indicate the structure of the scaffolds in the in-line projection images. Combining with the CT technique, both the scaffolds and the CMs can be visualized with recognizable contours of the structure.

Visualization of hydrogel scaffolds and encapsulated cells together in aqueous environments is promising for *in vivo* study for tissue engineering. Taking advantages of the parallel property of

the synchrotron beam, a possible way to combine images of hydrogel scaffolds and encapsulated cells was presented. Developed from the last results, PCI demonstrated high-quality images of the hydrogel scaffolds in water with high contrast at the contours. Long cross-linking time was the most important factor to enhance the contrast. Combined with tomography, the detailed inner structure of the scaffolds was revealed. Knowledge of this structure may be used for mechanics analysis to enhance structure design. The cells were proposed to be labeled with GNPs as contrast agent and imaged with absorption radiography. This method was able to demonstrate visible dark spots which possibly indicate the labeled cells. Overall, synchrotron-based PCI showed great potential for visualization of hydrogel scaffolds in high water-content environments. Better schemes for imaging cells in scaffolds still need to be developed in the future.

5.2 Limitations of present work

This study was subject to the following limitations:

1) For KES imaging, this work didn't include an evaluation of the cytotoxicity for both the physical and chemical techniques for incorporating barium.
2) The size of CMs used in the scaffold fabrication was not controlled, which led to blockage during the scaffold fabrication. With the settings used in the present study, the CMs are suggested being of 10~20 micron, i.e., 1/10 of the nozzle's diameter, in order to alleviate the problem of blockage.
3) The projection images of the GNPs label cells were not suitable for CT. Although some spots were observed in the radiography projections of the cell images, more details cannot be obtained to completely distinguish them from noise. Since the cell size (around 10 micron) is just a little bit larger than the detector resolution (4 micron), the potential cell image would occupy 2 or 3 pixels. The cells can hardly be distinguished from the noise unless the dark spots can be distributed in a certain pattern with higher contrast.

5.3 Future work

Due to the aforementioned limitations of the present work, the following studies are suggested.

Cell viability in the cross-linked scaffolds can indicate the toxicity of barium contrast agents. In order to obtain the cell viability, fluorescence staining can be employed. In traditional cell viability tests, the cells are stained in a liquid media, which can be dripped on a hemocytometer for cell counting. Hence, once the cells are encapsulated in cross-linked scaffolds with barium, cell staining becomes impossible. Fluorescence staining can be done before the encapsulation. After the scaffolds are cross-linked, cell viability can be obtained through microscope in three dimensions. Therefore, the cytotoxicity can be evaluated.

In the present work, the size of the CMs led to a serious blockage problem. In order to avoid blockage, the size of the fabricated CMs should be controlled. After obtaining the fluid properties of the alginate gel, finite element analysis can be applied to simulate the two-phase flow in the nozzle, and find the proper size of the particles. Smaller CMs can be fabricated with a higher rotary speed of the medium in a small container. The fabricated CMs can be checked though SEM to verify the size. Different settings of the 3D plotter can also be applied to make sure the alginate scaffolds with CMs can be fabricated.

Tomography can be applied for GNPs-labeled cells. Using the reconstruction algorithm, the CT images can show more details that may not be seen in the projections. In order to increase the contrast, edge absorption imaging can be applied for cell images as well. Since higher photon energy will be available at BMIT-ID, the K-edge and L-edge of gold can be achieved to enhance the contrast by subtraction of the images. After the cell images are available, the original idea of combining scaffolds' PCI image and cells' absorption image can be realized.

The possible future applications of these visualization techniques include structural analysis of the scaffolds and non-destructive *in vivo* observation of the scaffolds. Comparing with the

designed models, the fabricated scaffolds usually have some structural defects. CT images of the scaffolds can provide details of the inner structure which can be imported into finite element analysis software for mechanics simulation. The FEA can help to develop better fabrication schemes to reduce defects and improve mechanical properties. Also, after the scaffolds are implanted, how the alginate scaffolds enhance cell proliferation and self-degrade continuously *in vivo* can be observed by applying these synchrotron imaging methods.

REFERENCES

1. Guilak, F., et al., *The Pericellular Matrix as a Transducer of Biomechanical and Biochemical Signals in Articular Cartilage.* Annals of the New York Academy of Sciences, 2006. **1068**(1): p. 498-512.
2. Metters, A.T., K.S. Anseth, and C.N. Bowman, *A Statistical Kinetic Model for the Bulk Degradation of PLA-b-PEG-b-PLA Hydrogel Networks: Incorporating Network Non-Idealities.* The Journal of Physical Chemistry B, 2001. **105**(34): p. 8069-8076.
3. Zein, I., et al., *Fused deposition modeling of novel scaffold architectures for tissue engineering applications.* Biomaterials, 2002. **23**(4): p. 1169-1185.
4. Gibson, L.J. and M.F. Ashby, *Cellular Solids: Structure and Properties*1999: Cambridge University Press.
5. van Blitterswijk, C.A. and P. Thomsen, *Tissue Engineering*2008: Academic.
6. Peppas, N.A., et al., *Hydrogels in Biology and Medicine: From Molecular Principles to Bionanotechnology.* Advanced Materials, 2006. **18**(11): p. 1345-1360.
7. Nakamura, M., et al., *Biomatrices and biomaterials for future developments of bioprinting and biofabrication.* Biofabrication, 2010. **2**(1): p. 014110.
8. Nicodemus, G.D. and S.J. Bryant, *Cell encapsulation in biodegradable hydrogels for tissue engineering applications.* Tissue engineering. Part B, Reviews, 2008. **14**(2): p. 149-165.
9. Scott, E.A., et al., *Modular scaffolds assembled around living cells using poly(ethylene glycol) microspheres with macroporation via a non-cytotoxic porogen.* Acta Biomaterialia, 2010. **6**(1): p. 29-38.
10. Landers, R., et al., *Fabrication of soft tissue engineering scaffolds by means of rapid prototyping techniques.* Journal of Materials Science, 2002. **37**(15): p. 3107-3116.
11. DeKosky, B.J., et al., *Hierarchically designed agarose and poly(ethylene glycol) interpenetrating network hydrogels for cartilage tissue engineering.* Tissue engineering. Part C, Methods, 2010. **16**(6): p. 1533-1542.
12. Söntjens, S.H.M., et al., *Biodendrimer-Based Hydrogel Scaffolds for Cartilage Tissue Repair.* Biomacromolecules, 2005. **7**(1): p. 310-316.
13. Bryant, S.J., K.L. Durand, and K.S. Anseth, *Manipulations in hydrogel chemistry control photoencapsulated chondrocyte behavior and their extracellular matrix production.* Journal of Biomedical Materials Research Part A, 2003. **67A**(4): p. 1430-1436.
14. Shu, X.Z., et al., *Synthesis and evaluation of injectable, in situ crosslinkable synthetic extracellular matrices for tissue engineering.* Journal of Biomedical Materials Research Part A, 2006. **79A**(4): p. 902-912.
15. Rowley, J.A., G. Madlambayan, and D.J. Mooney, *Alginate hydrogels as synthetic extracellular matrix materials.* Biomaterials, 1999. **20**(1): p. 45-53.
16. Kataoka, K., et al., *Alginate enhances elongation of early regenerating axons in spinal cord of young rats.* Tissue engineering, 2004. **10**(3-4): p. 493-504.
17. Turco, G., et al., *Alginate/Hydroxyapatite Biocomposite For Bone Ingrowth: A Trabecular Structure With High And Isotropic Connectivity.* Biomacromolecules, 2009. **10**(6): p. 1575-1583.
18. Khalil, S. and W. Sun, *Bioprinting Endothelial Cells With Alginate for 3D Tissue Constructs.* Journal of Biomechanical Engineering, 2009. **131**(11): p. 111002-111002.

19. Landers, R., et al., *Rapid prototyping of scaffolds derived from thermoreversible hydrogels and tailored for applications in tissue engineering.* Biomaterials, 2002. **23**(23): p. 4437-4447.
20. Hendee, W., et al., *Bioengineering and Imaging Research Opportunities Workshop V: A Summary.* Annals of Biomedical Engineering, 2008. **36**(8): p. 1315-1321.
21. Zermatten, E., et al., *Micro-Computed Tomography Based Computational Fluid Dynamics for the Determination of Shear Stresses in Scaffolds Within a Perfusion Bioreactor.* Annals of Biomedical Engineering, 2014. **42**(5): p. 1085-1094.
22. Eshraghi, S. and S. Das, *Micromechanical finite-element modeling and experimental characterization of the compressive mechanical properties of polycaprolactone–hydroxyapatite composite scaffolds prepared by selective laser sintering for bone tissue engineering.* Acta Biomaterialia, 2012. **8**(8): p. 3138-3143.
23. Zhu, N., et al., *X-ray diffraction enhanced imaging as a novel method to visualize low-density scaffolds in soft tissue engineering.* Tissue engineering. Part C, Methods, 2011. **17**(11): p. 1071-1080.
24. Li, Z., et al., *Studies on the porous scaffold made of the nano-HA/PA66 composite.* Journal of Materials Science, 2005. **40**(1): p. 107-110.
25. Bhattarai, N., et al., *Electrospun chitosan-based nanofibers and their cellular compatibility.* Biomaterials, 2005. **26**(31): p. 6176-6184.
26. Lee, M., J.C.Y. Dunn, and B.M. Wu, *Scaffold fabrication by indirect three-dimensional printing.* Biomaterials, 2005. **26**(20): p. 4281-4289.
27. Bian, Y.-Z., et al., *Evaluation of poly(3-hydroxybutyrate-co-3-hydroxyhexanoate) conduits for peripheral nerve regeneration.* Biomaterials, 2009. **30**(2): p. 217-225.
28. He, L., et al., *The influence of laminin-derived peptides conjugated to Lys-capped PLLA on neonatal mouse cerebellum C17.2 stem cells.* Biomaterials, 2009. **30**(8): p. 1578-1586.
29. Bozkurt, A., et al., *In vitro cell alignment obtained with a Schwann cell enriched microstructured nerve guide with longitudinal guidance channels.* Biomaterials, 2009. **30**(2): p. 169-179.
30. Suzuki, E., *High-resolution scanning electron microscopy of immunogold-labelled cells by the use of thin plasma coating of osmium.* Journal of Microscopy, 2002. **208**(3): p. 153-157.
31. Muscariello, L., et al., *A critical overview of ESEM applications in the biological field.* Journal of Cellular Physiology, 2005. **205**(3): p. 328-334.
32. Pawley, J., *Handbook of Biological Confocal Microscopy*2006: Springer.
33. Sørensen, A., et al., *Long-term neurite orientation on astrocyte monolayers aligned by microtopography.* Biomaterials, 2007. **28**(36): p. 5498-5508.
34. Wosnick, J.H. and M.S. Shoichet, *Three-dimensional Chemical Patterning of Transparent Hydrogels.* Chemistry of Materials, 2007. **20**(1): p. 55-60.
35. Liu, C., Z. Xia, and J.T. Czernuszka, *Design and Development of Three-Dimensional Scaffolds for Tissue Engineering.* Chemical Engineering Research and Design, 2007. **85**(7): p. 1051-1064.
36. Mironov, V., et al., *Organ printing: computer-aided jet-based 3D tissue engineering.* Trends in Biotechnology, 2003. **21**(4): p. 157-161.
37. Sun, W., et al., *Bio-CAD modeling and its applications in computer-aided tissue engineering.* Computer-Aided Design, 2005. **37**(11): p. 1097-1114.

38. Whaites, E. and N. Drage, *Essentials of Dental Radiography and Radiology*2013: Elsevier Science Health Science Division.
39. Sokolov, A.A., I.M. Ternov, and C.W. Kilmister, *Radiation from relativistic electrons*1986: American Institute of Physics.
40. Herman, G.T., *Fundamentals of Computerized Tomography: Image Reconstruction from Projections*2012: Springer Verlag.
41. Cullerne, J. and J. Daintith, *The Penguin Dictionary of Physics*2000: Penguin.
42. Peterzol, A., et al., *Performance of the K-edge digital subtraction angiography imaging system at the European synchrotron radiation facility.* Radiation Protection Dosimetry, 2005. **117**(1-3): p. 44-49.
43. Schültke, E., et al., *The potential for neurovascular intravenous angiography using K-edge digital subtraction angiography.* Nuclear Instruments and Methods in Physics Research Section A: Accelerators, Spectrometers, Detectors and Associated Equipment, 2005. **548**(1–2): p. 84-87.
44. Lawaczeck, R., et al., *New Contrast Media Designed for X-Ray Energy Subtraction Imaging in Digital Mammography.* Investigative Radiology, 2003. **38**(9): p. 602-608.
45. de Vos, P., et al., *Alginate-based microcapsules for immunoisolation of pancreatic islets.* Biomaterials, 2006. **27**(32): p. 5603-5617.
46. Zekorn, T., et al., *Barium-cross-linked alginate beads: a simple, one-step method for successful immunoisolated transplantation of islets of Langerhans.* Acta Diabetologica, 1992. **29**(2): p. 99-106.
47. Kono, M., et al., *Refraction Imaging and Histologic Correlation in Excised Tissue from a Normal Human Lung: Preliminary Report.* Academic Radiology, 2001. **8**(9): p. 898-902.
48. Arhatari, B.D., et al., *Phase contrast radiography: Image modeling and optimization.* Review of Scientific Instruments, 2004. **75**(12): p. 5271-5276.
49. Liu, P., et al., *Morphological study of early-stage lung cancer using synchrotron radiation.* Journal of synchrotron radiation, 2008. **15**(Pt 1): p. 36-42.
50. Liu, P., et al., *Detection of lung cancer with phase-contrast X-ray imaging using synchrotron radiation.* Conference proceedings : ... Annual International Conference of the IEEE Engineering in Medicine and Biology Society. IEEE Engineering in Medicine and Biology Society. Conference, 2006. **1**: p. 2001-2004.
51. Sun, W., et al., *Experimental study on phase-contrast imaging with synchrotron hard X-ray for repairing osteonecrosis of the femoral head.* Orthopedics, 2011. **34**(9): p. e530-4.
52. Cedola, A., et al., *Three dimensional visualization of engineered bone and soft tissue by combined x-ray micro-diffraction and phase contrast tomography.* Physics in Medicine and Biology, 2014. **59**(1): p. 189.
53. Marenzana, M., et al., *Synchrotron- and laboratory-based X-ray phase-contrast imaging for imaging mouse articular cartilage in the absence of radiopaque contrast agents.* Philosophical Transactions of the Royal Society A: Mathematical, Physical and Engineering Sciences, 2014. **372**(2010).
54. Baruchel, J., et al., *Phase-contrast imaging of thin biomaterials.* Biomaterials, 2001. **22**(12): p. 1515-1520.
55. Rustichelli, F., et al., *Phase-contrast microtomography of thin biomaterials.* Journal of Materials Science: Materials in Medicine, 2004. **15**(9): p. 1053-1057.
56. Brey, E.M., et al., *X-ray imaging of poly(ethylene glycol) hydrogels without contrast agents.* Tissue engineering. Part C, Methods, 2010. **16**(6): p. 1597-1600.

57. Thurner, P., et al., *Tomography studies of biological cells on polymer scaffolds.* Journal of Physics: Condensed Matter, 2004. **16**(33): p. S3499.
58. Menk, R.H., et al., *Gold nanoparticle labeling of cells is a sensitive method to investigate cell distribution and migration in animal models of human disease.* Nanomedicine: Nanotechnology, Biology and Medicine, 2011. **7**(5): p. 647-654.
59. Astolfo, A., et al., *A detailed study of gold-nanoparticle loaded cells using X-ray based techniques for cell-tracking applications with single-cell sensitivity.* Nanoscale, 2013. **5**(8): p. 3337-3345.
60. Astolfo, A., et al., *In vivo visualization of gold-loaded cells in mice using x-ray computed tomography.* Nanomedicine: Nanotechnology, Biology and Medicine, 2013. **9**(2): p. 284-292.
61. Zehbe, R., et al., *Going beyond histology. Synchrotron micro-computed tomography as a methodology for biological tissue characterization: from tissue morphology to individual cells.* Journal of The Royal Society Interface, 2010. **7**(42): p. 49-59.
62. Giuliani, A., et al., *Polyglycolic Acid-polylactic Acid scaffold response to different progenitor cell in vitro cultures: a demonstrative and comparative x-ray synchrotron radiation phase-contrast microtomography study.* Tissue engineering. Part C, Methods, 2014. **20**(4): p. 308-316.
63. Mørch, Ý.A., I. Donati, and B.L. Strand, *Effect of Ca2+, Ba2+, and Sr2+ on Alginate Microbeads.* Biomacromolecules, 2006. **7**(5): p. 1471-1480.
64. Winkler, A.W., H.E. Hoff, and P.K. Smith, *Cardiovascular Effects of Potassium, Calcium, Magnesium, and Barium: An Experimental Study of Toxicity and Rationale of Use in Therapeutics.* The Yale journal of biology and medicine, 1940. **13**(1): p. 123-132.
65. Chen, X., et al., *Novel Sulfated Glucomannan-Barium-Alginate Microcapsules in Islet Transplantation: Significantly Decreased the Secretion of Monocyte Chemotactic Protein 1 and Improved the Activity of Islet in Rats.* Transplantation Proceedings, 2009. **41**(10): p. 4307-4312.
66. Safley, S.A., et al., *Biocompatibility and Immune Acceptance of Adult Porcine Islets Transplanted Intraperitoneally in Diabetic NOD Mice in Calcium Alginate Poly-L-lysine Microcapsules versus Barium Alginate Microcapsules without Poly-L-lysine.* Journal of Diabetes Science and Technology, 2008. **2**(5): p. 760-767.
67. Sinha, V.R., et al., *Chitosan microspheres as a potential carrier for drugs.* International Journal of Pharmaceutics, 2004. **274**(1–2): p. 1-33.
68. Lao, L., et al., *Chitosan modified poly(l-lactide) microspheres as cell microcarriers for cartilage tissue engineering.* Colloids and Surfaces B: Biointerfaces, 2008. **66**(2): p. 218-225.
69. Niu, X., et al., *Porous nano-HA/collagen/PLLA scaffold containing chitosan microspheres for controlled delivery of synthetic peptide derived from BMP-2.* Journal of Controlled Release, 2009. **134**(2): p. 111-117.
70. Frens, G., *Controlled nucleation for the regulation of the particle size in monodisperse gold suspensions.* Nature, 1973. **241**(105): p. 20-22.
71. Juurlink, B.H.J. and R.M. Devon, *Colloidal gold as a permanent marker of cells.* Experientia, 1991. **47**(1): p. 75-77.